A Boosted Machine Learning Framework for the Improvement of Phase and Crystal Structure Prediction of High Entropy Alloys Using Thermodynamic and Configurational Parameters

Debsundar Dey[1], Suchandan Das[2], Anik Pal[3], Santanu Dey[4], Chandan Kumar Raul[4*], Arghya Chatterjee[4*]

[1]Department of Materials Engineering, Indian Institute of Science, Bengaluru-560012, India

[2]Department of Electrical Engineering, National Institute of Technology, Silchar- 788010, India

[3]Department of Physics, Ramananda college, Bishnupur-722122, India

[4]Department of Physics, National Institute of Technology, Durgapur-713209, India

[*]Corresponding authors. E-mail addresses: ckr.19ph1102@phd.nitdgp.ac.in (C. K. Raul), achatterjee.phy@nitdgp.ac.in (A. Chatterjee) .

Abstract:

The reason behind the remarkable properties of High-Entropy Alloys (HEAs) is rooted in the diverse phases and the crystal structures they contain. In the realm of material informatics, employing machine learning (ML) techniques to classify phases and crystal structures of HEAs has gained considerable significance. In this study, we assembled a new collection of 1345 HEAs with varying compositions to predict phases. Within this collection, there were 705 sets of data that were utilized to predict the crystal structures with the help of thermodynamics and electronic configuration. Our study introduces a methodical framework i.e., the Pearson correlation coefficient that helps in selecting the strongly co-related features to increase the prediction accuracy. This study employed five distinct boosting algorithms to predict phases and crystal structures, offering an enhanced guideline for improving the accuracy of these predictions. Among all these algorithms, XGBoost gives the highest accuracy of prediction (94.05%) for phases and LightGBM gives the highest accuracy of prediction of crystal structure of the phases (90.07%). The quantification of the influence exerted by parameters on the model's accuracy was conducted and a new approach was made to elucidate the contribution of individual parameters in the process of phase prediction and crystal structure prediction.

Keywords: High entropy alloy; Machine Learning; Feature selection; Phase prediction; Crystal structure

1 Introduction:

HEAs, also known as multi-principal elemental alloys (MPEAs), represent an innovative and cutting-edge approach to advanced material design and development. Contrary to conventional alloys that rely on one or two main elements, HEAs comprise multiple principal elements in nearly equal atomic ratios. HEA can be defined as an alloy that contains five or more principal elements containing the atomic percentage of each minor element 5% to 35%. The condition of HEAs in the entropy-based approach for equ-atomic elements is $\Delta S_{config} > 1.5R$ where R is the universal gas constant [1].

This unique alloy fabrication concept has revolutionized the field, enabling the creation of a wide range of compositions with diverse combinations of desirable properties such as high corrosion resistance, high wear resistance, excellent specific strength, desirable mechanical performance at elevated temperatures, exceptional ductility, and fracture resistance capacity at cryogenic temperatures [2]. The unusual excellent properties shown by the HEAs largely depend upon the phases present in the alloys such as solid solution (SS), intermetallic compounds (IM), solid solution + intermetallic (SS+IM), and amorphous (AM). Therefore, it becomes very important to predict the phases or combination of phases of HEAs for their better engineering application [3]. The superior properties of HEAs are primarily attributed to their SS phase, which is believed to be the main contributing factor [4]. However, the presence of a brittle IM phase in the alloy can negatively affect its ductility characteristics [5]. In comparison, single-phase HEAs with a body-centered cubic (BCC) structure exhibit high strength but tend to be brittle, while single-phase HEAs with a face-centered cubic (FCC) structure are typically ductile but have low strength. So, predicting phases of HEAs navigates to design HEAs with novel properties which can have both the combination of strength and ductility which most of the materials engineers look for. The study conducted by Guo et al. provided important new insight regarding the prediction of phase formation in high-entropy alloys [6]. According to their study valence electron concentration (VEC) is an important parameter to decide the phases of HEAs. If VEC>8, it gives rise to the BCC phase and whenever VEC<6.87, it gives rise to the FCC phase [7]. Franz Karl Achard was the first person to study multi-component equ-mass alloys with five to seven elements [8]. Cantor et al.

first studied the $Fe_{20}Cr_{20}Ni_{20}Mn_{20}Co_{20}$ alloy which can hold 20 different components each at 5% and forms FCC structure [9]. In a groundbreaking development, researchers have employed the adaptive neuro-fuzzy interface system (ANFIS) to make phase predictions in HEAs, marking the first-ever utilization of artificial intelligence in this field. The predictions were conducted through two distinct methodologies. In the first one, the composition of the elements was considered as inputs, and in the second case six parameters were used which were proven as very important parameters for forming the alloys [9]. Yeh et al. studied that mixing entropy is an important parameter to increase the mixing probability of the principal elements and reduce the phases present in the alloy [10]. Huang et al. introduced a novel ML approach to predict the occurrence of solid solution or intermetallic formations in HEAs with an accuracy level of more than 70% [11]. Guo et al. and Zhang et al. conducted calculations for the prediction of SS and IM formation in HEAs and they established that electronegativity difference ($\Delta\chi$) and valence electron concentration (VEC), are crucial for understanding and correlating the properties of HEAs [12]. Islam et al. used neural network to classify HEAs into SS, IM, and AM using five parameters as inputs where they got 90% accuracy for training data and an average cross-validation (4-fold) accuracy of 83% [13]. Huang et al. [11] performed phase classification using the dataset of Miracle et al. [14] of HEAs using three algorithms such as k-nearest neighbor (k-NN), support vector machine (SVM), and artificial neural network (ANN). In their study, five input features were utilized for the classification of three phases. The reported accuracies were 68.6% for k-NN, 64.3% for SVM, and 74.3% for ANN. These results indicate that ANN outperformed the other algorithms, demonstrating its superiority in classifying HEA phases. Zhang et al. performed classification problems using genetic algorithm which helped to predict the phases of HEAs i.e., SS and non-solid solution (NSS) with test accuracy of 88.7% using neural network algorithm respectively [15]. It is very well established in metallurgy i.e.; the formation of SS follows the Hume-Rothery rule [16]. It states the importance of four parameters crystal structure, radius difference, electronegativity difference, and valency which largely decide the condition of the formation of SS. Machaka et al. compared the performance of two machine learning algorithms, namely decision tree and random forest, for the classification of phases in HEAs. The classification task involved distinguishing between FCC, BCC, FCC + BCC, and IM phases. The findings indicated that random forest achieved superior results in phase classification, exhibiting a test accuracy of 82.3% [17]. Currently, Troparevsky et al. used the formation enthalpies of binary intermetallic

compounds to predict the combinations of elements that can form single-phase alloys [18]. As an alternative, phase stability has been calculated using the CALPHAD approach and first-principles calculations, which have proven to be more reliable [19-23]. Senkov et al. sorted out more than 1000 MPEAs with different compositions promising for high-temperature structural applications using powerful CALPHAD simulations [24]. The CALPHAD approach, however, is insufficient for alloys composed of more than five elements and is restricted to small numbers of components [25]. First-principles calculations do not rely on experimental data, but they are computationally very expensive and time-consuming to run for MPEAs. Consequently, a new computational approach is considered to predict the phases of HEAs which expedite the discovery and design of new materials. With the rising popularity of MPEAs, there is a pressing need to develop dependable tools capable of reliably predicting the diverse phases that arise in MPEAs [26]. ML offers inherent advantages over traditional modeling techniques due to its ability to adapt to new data and efficiently establish relationships between input data and desired outcomes [27]. Kaufmann et al. proposed a novel high-throughput approach called "ML-HEA" that integrates chemical and thermodynamic properties [28]. Researchers have investigated combining physical models with data-driven models to achieve desired results which provide them with good results in a wide range. However, the existing literature rarely delves into the aspect of recommending an optimal algorithm for the prediction of phases and crystal structures of HEAs with high accuracy [29]. Still, there is vast scope to improve the accuracy of prediction of phase formation and crystal structure prediction as well as feature selection. Since the phase production method for HEAs is arbitrary and does not follow a specific rule, there is no typical conventional way to expose the entire phase formation mechanism. Pritam et al. conducted a study for phase prediction of HEAs where they achieved 93.84% accuracy for phase prediction using decision tree (DT) and SVM, and 84.32% accuracy for crystal structure prediction using SVM [30].

In this study, ML plays a crucial role to correlate the input features with the output which is experimentally very difficult to establish. Here we employ ML algorithms to explore phase selection conditions using a comprehensive experimental dataset of 1345 different HEAs including SS, IM, SS + IM, and AM phases. We have also classified the 705 datasets into four different classes such as BCC, FCC, BCC+FCC, and multiphase to predict the crystal structures. Here our study suggests a new approach to predict the phases and crystal structures with greater accuracy with the help of five boosting algorithms which was not reported previously. In our study, we have

employed different ML approaches such as XGBoost, Gradient boosting, AdaBoost, LightGBM, and CatBoost which appear to be very time efficient and widely recognized for complex feature extraction.

2 Computational methods:

2.1 Data collection:

We have used 1345 datasets collected from different open-source literature [31-39] and from the review article on HEAs by Miracle and Senkov for the prediction of the phases of HEAs and 705 datasets for the prediction of the crystal structure [15]. Our dataset consists of 535 SS, 276 IM, 328 SS+IM, and 206 AM out of 1345 data, and 213 BCC, 135 FCC, 82 FCC+BCC, and 275 multiphase out of 705 data, which comprise FCC+HCP, FCC + Laves phase, FCC + boride + unknown phase, etc. Some of the data of phases and crystal structures of high entropy alloys are provided in Tables 1 and 2. In our study, we have used five important thermodynamic and configurational parameters which have been employed as input features to predict the stable phases and crystal structure of HEAs. The five input parameters and their equation to get the numerical values are mentioned below in equation numbers 1-5.

$$VEC = \sum_{i=-1}^{n} C_i \, VEC_i \tag{1}$$

$$\Delta\chi = \sqrt{\sum_{i=1}^{n} C_i (\chi - \bar{\chi})^2} \tag{2}$$

$$\delta = 100 \times \sqrt{\sum_{i=1}^{n} C_i \left(1 - r_{i/\bar{r}}\right)^2} \tag{3}$$

$$\Delta S_{\text{mix}} = -R \sum_{i=1}^{n} C_i \ln C_i \tag{4}$$

$$\Delta H_{\text{mix}} = -R \sum_{i=1, i<j}^{n} 4 H_{ij} \, C_i \, C_j \tag{5}$$

Here, VEC represents the valence electron concentrations, $\Delta\chi$ represents electronegativity difference, δ denotes atomic radius, ΔS_{mix} and ΔH_{mix} represent mixing entropy and mixing enthalpy respectively, while C_i represents the atomic concentrations of the i^{th} element. The variable 'n' represents the total number of different elements present in HEAs. The symbol χ_i denotes the Pauling electronegativity of the i^{th} element, and r_i represents the radius of the i^{th} element. The average Pauling electronegativity $\bar{\chi}$ can be calculated as $\bar{\chi} = \sum_{i=1}^{n} C_i \chi_i$ and the

average radius can be evaluated as $\bar{r} = \sum_{i=1}^{n} c_i r_i$. Here, H_{ij} refers to the enthalpy of atomic pairs between the i^{th} and j^{th} elements, which has been determined using the Miedema method by Takeuchi and Inoue [11,40].

2.2 Data balancing using SMOTE:

To overcome the problem of unbalanced data, we suggest employing the SMOTE (Synthetic Minority Over-Sampling Technique) algorithm in this study [41,42]. The SMOTE algorithm starts by randomly selecting an instance from the minority class, denoted as X_{ki}. It then identifies the k nearest neighbors among the minority class instances. The next step is to create a synthetic instance by picking one of these k neighbors at random X_i and connecting it to X_{ki} in the feature space to create a line segment. The synthetic instances are created by combining X_{ki} and X_i in a convex manner [43].

This can be mathematically represented as: $X_n = X_i + \lambda (X_{ki} - X_i)$, where X_n represents the newly created synthetic sample, and λ is a random number between 0 and 1 [44]. The synthetic samples can be incorporated into the training set since they are produced nearby the original samples in the feature space. In this study, the dataset was obtained and the SMOTE approach was used to pre-process the data before feature extraction. By oversampling the minority class using SMOTE, the disparity between the minority and majority classes was removed which was one of the main objectives. We attempted to improve the balance of the given dataset by increasing the amount of data instances in the minority class. In Fig. 1.a, b and Fig. 2.a, b it is shown how the data were oversampled by SMOTE by generating synthetic samples for minority class and removes the imbalances of the data. Fig. 1.a and Fig. 2.a show the imbalanced data whereas Fig. 1.b and Fig. 2.b indicate the balanced data after using SMOTE technique. Here, Fig. 1,2 show the application of principal component analysis for reducing the multi-dimension plotting to two-dimension plotting for prediction of phases and crystal structures.

2.3 Feature selection using Pearson correlation coefficient:

The ability of ML models to predict outcomes accurately is substantially influenced by the characteristics chosen. while adding more features can enhance the information available to the algorithm, redundant features can saturate the algorithm with excessive or duplicated information. The Pearson correlation coefficient is a useful tool in identifying and addressing this redundancy,

ensuring that the model focuses on the most relevant and distinct information from the available features. Therefore, it is crucial to eliminate extremely comparable characteristics in order to prevent the catastrophe of dimensionality and achieve the best classification accuracy [45].

Pearson correlation coefficient not only indicates the direction of the relation of the considered features but also indicates how strongly the feature is correlated with a quantitative analysis. This helps in removing the unnecessary feature and increasing the accuracy of the algorithm [46]. In our work, we have set the threshold value of the Pearson correlation coefficient as 0.8 (which indicated features are strongly correlated). From Fig. 3, it can be seen that δ (%) and Δχ are strongly correlated. Only those features are taken, that have correlation coefficients less than 0.8. In this study, the Pearson correlation coefficient is 0.92 for $\Delta\chi$ and δ (%). That's why in ML models only $\Delta\chi$ is considered and the δ (%) feature is removed for predicting the phases and crystal structure. Therefore, our working features are VEC, $\Delta\chi$, ΔH_{mix} (kJ/mol), and ΔS_{mix} (J/ (mol · K). In Fig. 3.a, the five features are taken into consideration. Fig. 3.b shows the selection of features using the Pearson correlation coefficient which clearly indicated δ (%) and $\Delta\chi$ have a strong correlation for which reason the algorithm automatically removes the δ (%) feature as it has the same impact over the prediction model and it also helps in increasing the prediction accuracy with the help of fewer features of the model.

2.4 Data analysis with the help of scatter matrix plot:

In Fig. 4 and 5**,** the dataset is depicted through the 4×4 scatter matrix plot. The scatter plot is generated by the Python seaborn package. In both the diagram, the connection between the feature parameters used in the dataset are correlated which are used to predict the phases and crystal structures. The diagonal subgraphs show the intercorrelation of each feature i.e., all four features are important to predict the phases and the crystal structure of HEAs as all the diagonal subgraphs cannot be isolated from each other. The off-diagonal subgraphs show the overall pattern of the data. This plot indicates that only one single feature cannot predict the phases and crystal structures of HEAs.

2.5. Machine learning algorithms:

Advances in science and technology have been essential to the growth and development of alloy modeling, design, and property prediction. ML techniques have surfaced in several academic domains in recent years. However, variances in prediction accuracy can be seen because each ML

algorithm's application and operating principles differ. Programmable algorithms are used by ML algorithms to analyze input data and predict output values within a certain domain. These algorithms gradually build intelligence as they learn from freshly added data with each iteration and optimize their operations to improve performance. The following boosting ML algorithms are used to approach the problem of the prediction of phases and crystal structure of HEAs [47,48].

2.5.1 XGBoost:

The training error with the regularization can be combined to form the goal function of XGBoost. This definition captures the equilibrium between accurately fitting the training data and managing the model's complexity [49]. The mathematical expressions are explained below.

$$F = \sum_i L(\hat{z}_i, z_i) + \sum_k \beta(f_k) \quad (6)$$

$$\beta(f) = \gamma T + \frac{1}{2}\lambda \parallel \mu \parallel^2 \quad (7)$$

Here, F is the objective function. The loss function tracks how far the projected values deviate from the actual values. The regularization function β measures the training model's complexity to prevent overfitting. T denotes the overall number of leaf nodes, and μ denotes the score assigned to each leaf node. To prevent overfitting, the regulating parameters γ and λ are used [50]. Calculating the predicting score $\hat{z}^{(m-1)}$ of the m^{th} tree and finally the objective function can be written as:

$$F^{(m)} = \sum_{i=1}^{n} L\left(z_i, \hat{z}^{(m-1)} + f_t(x_i)\right) + \beta(f_m) \quad (8)$$

A second-order Taylor polynomial of $f_m = 0$ replaces an appropriate function f_m and the predicted objective function can be written as:

$$F^{(m)} = \sum_{i=1}^{n} \left[L\left(z_i, \hat{z}^{(m-1)}\right) + a_i f_m(x_i) + \frac{1}{2} b f_m^2(x_i)\right] + \beta(f_m) \quad (9)$$

$$a_i = \partial_{\hat{z}^{(m-1)}} L\left(z_i, \hat{z}^{(m-1)}\right) \text{ and } b_i = \partial^2_{\hat{z}^{(m-1)}} L\left(z_i, \hat{z}^{(m-1)}\right) \quad (10)$$

Here, $a_i$indicates the first-order derivative and b_i denotes the second-order derivative:

$$F^{(m)} = \sum_{i=1}^{n} \left[a_i f_m(x_i) + \frac{1}{2} b_i f_m^2(x_i)\right] + \beta(f_m) \quad (11)$$

$$\text{If } L_i = \{i \mid q(x_i) = j\}$$

Once the classification process is complete, the instances within the dataset are grouped based on their assigned leaf nodes, allowing for the reassembly of instances that share the same leaf node and can be expressed as:

$$F^{(m)} = \sum_{j=1}^{T} \left[\left(\sum_{i \in I_j} a_i \right) W_j + \frac{1}{2} \left(\sum_{i \in I_j} b_i + \lambda \right) W_j^2 \right] + \gamma \quad (12)$$

Finally, the optimum W and objective function can be written as [51]:

$$W_j^* = -\frac{\sum_{i \in I_j} a_i}{\sum_{i \in I_j} b_i + \lambda} \quad (13)$$

$$F^{(m)}(q) = -\frac{1}{2} \sum_{j=1}^{T} \frac{\left(\sum_{i \in I_j} a_i \right)^2}{\sum_{i \in I_j} b_i + \lambda} + \gamma T \quad (14)$$

Here,

$$\hat{z} = \phi(x_i) = \sum_{k=i}^{K} f_k(x_i) \quad (15)$$

$$f_k(x_i) = W_{q(x)}, f_k \in \mathcal{F} \quad (16)$$

The number of trees is indicated by $f_k(x_i)$ which converts the input x_i into the output for k^{th} tree; The score of each leaf node is denoted by $W_{q(x)}$; The number of leaf nodes is indicated by $q(x)$: $\mathcal{F}$ forms a collection of all corresponding functions f_k, representing the ensemble of models created during the XGBoost algorithm [52]. In our study, the learning rate is 0.01, the n-estimator is 200, the maximum depth is 5, subsample fraction is 0.8.

2.5.2 AdaBoost:

AdaBoost, short for Adaptive Boosting, is one of the first and most popular boosting algorithms. It was introduced by Yoav Freund and Robert Schapire [53]. The AdaBoost model is an iterative method that turns the learning process into an optimization challenge by combining several weak classifiers to generate a powerful classifier [54]. AdaBoost greatly raises classification accuracy by giving the poor classifiers a chance to strengthen their data fit. This approach can be used for a variety of ML applications because it is simple to develop [55]. Notably, AdaBoost exhibits remarkable accuracy while lowering the likelihood of overfitting. It consequently becomes a reliable and effective method for addressing a variety of classification issues in the field of ML.

AdaBoost gives the incorrectly classified samples additional weight in each iteration, encouraging the next weak classifiers to concentrate more on accurately identifying those challenging cases. As a result, the final strong classifier which greatly enhances classification accuracy, is a weighted combination of the weak classifiers.

Mathematically,

In each iteration of AdaBoost, the normalized factor can be written as**:**

$$Y_t = \sum_{i=1}^{m} D_t(i)\exp\left(-\alpha_t y_i h_t(x_i)\right) \quad (17)$$

Here, $D_t(i)$ is the distribution of the weight used over the all-training data, α_t is the parameter which helps to update $D_t(i)$; $y_i \in$ {-1, +1} where +1 represents merge while -1 represents the splitting; h_t is the weak hypothesis [56].

In our study, the value of learning rate is 0.01 and the n-estimator (the number of weak learners used in the dataset) is assigned as 200. The maximum depth of the algorithm is assigned as 3 and the minimum sample leaf and sample split are 1 and 2 respectively.

2.5.3 Gradient boosting:

Gradient boosting, as introduced by Friedman in 2002, is a powerful technique for building additive regression and classification models [57]. It works iteratively by utilizing least squares to fit a straightforward function (base learner) to the current "pseudo" residuals at each stage by adding a decision tree. The gradient of the loss function relating to the model predictions at each training data point, as determined at the current iteration, is represented by these “pseudo” residuals [58].

By successively introducing additional decision trees, commonly referred to as "weak learners," the GBM algorithm iteratively improves the model in order to reduce the loss function. The initial model for regression problems is typically a decision tree that minimizes the loss function, which in the context of regression is frequently the mean squared error. The algorithm iteratively improves the model, reducing the residual error and raising the model's overall performance with each iteration. Due to its iterative structure, GBM can incrementally build decision trees that focus on the remaining errors, improving the model's ability to predict outcomes.

The steps are illustrated below:

i. The control parameter can be set manually such as the decision tree depth (d), the number of iterations (n), the learning rate (α), and the subsample fraction (Ɛ).

ii. The residual value is set as $r_0 = z$ and $\widehat{F} = 0$. The mean value of z is set according to the starting guess of $\hat{F}$ [59].

iii. For the different n values where $n = 1,2,3,4, \dots, n$

a. A subsample $\{z_i, x_i\}^{k'}$ is selected randomly from the training dataset where k' is the dataset corresponding to Ɛ

b. Using $\{z_i, x_i\}^{k'}$ fit a decision tree of depth d to the residual r_{n-1}

c. decision is added to the model [60]:

$$\hat{F}(x) \leftarrow \hat{F}(x) + \alpha\, \hat{F}^n(x) \tag{18}$$

d. Residual is updated: $r_n \leftarrow r_{n-1} \times \alpha\, \widehat{F}^n(x)$ (19)

Here, the hyperparameters such as learning rate α is assigned as 0.001, maximum depth (d) as 9, minimum sample leaf as 6, and subsample fraction (Ɛ) as 0.85.

2.5.4 LightGBM:

'Light' refers to high speed which indicates it can handle large amounts of data within less time. LightGBM is a consolidation framework that uses the decision tree method and is very effective and quick. It is frequently used in automated learning tasks, including as classification and organization. Notably, LightGBM greatly decreases the training time as compared to XGBoost, making it particularly beneficial when working with huge dataset [61]. The main difference between LightGBM and XGBoost is how they approach algorithms. Faster training is achieved through LightGBM histogram-based technique, which discretizes continuous features into discrete intervals [62]. The mechanism used by the framework depends on a leaf-wise tree growth that converges quickly. However, it requires meticulous consideration to prevent the problem of overfitting [63]. The objective function can be calculated by the equation mentioned below:

$$z^n = z^{n+1} + f_n(x_i) \tag{20}$$

$$o^{(n)} = \sum_{i=1}^{k} L(z_i, z_i^n) + \sum_{i=1}^{k} \delta(f_i) \quad (21)$$

Here, f_i is the decision tree, $\delta(f_i)$is indicated as the regular term, L is the loss function, k is the total number of samples of the data, n is termed as the number of iterations and i is the sample from 1 to k [64]. In our study, the learning rate is 0.01 and n-estimator is 100, maximum depth is 1, number of leaves are 31.

2.5.5 CatBoost:

CatBoost, introduced by Dorogush et al. in 2018 [65], is an advanced GBDT toolkit, akin to XGBoost. This framework effectively addresses gradient bias and prediction shift issues offering several notable advantages. CatBoost is a method that combines category characteristics with GBDT to produce a better implementation of GBDT. Effectively managing categorical features is a major difficulty. By fusing boosting and categorical variables, CatBoost addresses this issue. It also addresses gradient bias and prediction shift concerns, improving the algorithm's resilience and generalizability in the process. CatBoost first determines the target value for the sample before numerically changing the features of each sample. When processing the sample, it then integrates the appropriate weight and priority. The equation is shown below

$$z_k^i = \frac{\sum_{j=1}^{n} \{z_j^i = z_k^i\} \cdot w_i + bp}{\sum_{j=1}^{n} \{z_j^k = z_k^i\} + b} \quad (22)$$

Here, $b > 0$ is a parameter. A common setting for p is the average target value in the dataset [66-67]. Here, the learning rate is 0.01 and n-estimator is 100, maximum depth is 4, number of leaves are 32.

2.6 Methodology:

To establish an ML framework, the initial stage involves ensuring the accessibility of input parameters. Using thermodynamic and configurational parameters as model inputs, phase prediction and crystal structure determination were successfully accomplished in this study. The input parameters are VEC, $\Delta\chi$, ΔH_{mix} , ΔS_{mix} where ΔH_{mix} is a thermodynamic parameter that helps in governing the phase formation rule, and mixing configurational entropy (ΔS_{mix}) quantifies the number of possible microstates that correspond to a particular macrostate of the system. The flow diagram is shown here in Fig. 6 which shows that after collecting imbalanced data from different sources, SMOTE was used to make the dataset balanced. After balancing the data,

Pearson correlation coefficient was applied to select the necessary feature and to remove strongly correlated features to improve the accuracy of the model. Different boosting ML algorithms were used to predict the phases and crystal structures of HEAs. The performance of the model was evaluated by four parameters such as accuracy (%), recall (%), precision (%), and F1 score.

In order to predict the phases and crystal structures of HEAs, we conducted a specific exploration of boosting algorithms to enhance the accuracy of our predictions. This aspect had not been previously reported in other studies. Our findings demonstrate that the chosen boosting algorithms not only significantly improved prediction accuracy but also proved to be more time-effective in comparison to alternative methods.

By computing statistical measures like true positives (TP), true negatives (TN), false positives (FP), and false negatives (FN), any binary classification problem can be evaluated for their accuracy. The confusion matrix was applied to a detailed breakdown of the classifier's performance for each crystal phase selection category, allowing us to identify both correct and incorrect predictions. The confusion matrix, or confusion score, summarizes how well the classifier distinguishes between positive and negative events in the dataset [68]. Table 3 shows the binary classification using the confusion matrix. The accuracy can be calculated as follows:

$$Accuracy\ (\%) = \frac{TP+TN}{FP+FN+TP+TN} \times 100 \quad (23)$$

A brief description is given of the performance evaluator of the model. Precision is a key metric in classification tasks, representing the ratio of correctly identified positive instances out of all positively predicted cases. It is calculated as the division of true positive predictions by the sum of true positive and false positive predictions. In other words, it assesses the model's capacity to prevent false positives and generate precise positive results by measuring the accuracy of positive predictions made by the model [69]. Precision is defined by:

$$Precision\ (\%) = \frac{TP}{TP+FP} \times 100 \quad (24)$$

Recall, which is often referred to as sensitivity or true positive rate, quantifies the percentage of real positive events that the model accurately recognized. It measures how well the model can identify every single positive example from the whole collection of positive data [70]. It can be defined as:

$$Recall\ (\%) = \frac{TP}{TP+FN} \times 100 \quad (25)$$

$F1\ score$ is a single metric that combines recall and precision to give a fair evaluation of the effectiveness of a classification algorithm. It determines the harmonic mean of recall and precision, providing a mechanism to take both false positives and false negatives into consideration [71]. Mathematically it can be written as:

$$F1\ score\ = \frac{2 \times Precision \times Recall}{Precision+Recall} \quad (26)$$

In the below Tables 4 and 5, recall, precision, and F1 score are given for the prediction of phases and crystal structure respectively.

The performance of our model is also evaluated graphically using the Receiver Operating Characteristic (ROC) curve. It offers insightful statistical data on the equilibrium between sensitivity and specificity for various threshold settings [72]. Specificity corresponds to the false positive rate (FPR), whereas sensitivity represents the true positive rate (TPR). The model is initially trained before the probability threshold for categorizing data as positive which are varied from high to low to create the ROC curve [73]. The model's performance under each threshold is represented as a point on the curve, demonstrating the model's capacity to recognize the positive and negative instances. It illustrates how well the model distinguishes between positive and negative samples, highlighting the trade-off between correctly identifying positive cases (sensitivity) and incorrectly classifying negative cases as positive.

Here TPR is defined as: $TPR = \frac{TP}{TP+FN}$ and FPR is defined as: $FPR\ = \frac{FP}{FP+TN}$. True positive rate and recall indicate the same mathematical quantity [74]. A common statistic for assessing binary classification systems is area under the curve (AUC). The area under the ROC curve was used to compute this AUC value. The AUC serves as an essential indicator of the classifier's accuracy and ability to recall positive instances.

In prior investigations, it was demonstrated that a set of five parameters played a significant role in accurately predicting both the phases and crystal structure. However, through the utilization of the Pearson correlation coefficient, we have now revealed that a reduced set of only four parameters suffices to effectively achieve our objective while still maintaining a high level of predictive accuracy.

3 Results and discussions:

It is impractical to use the conventional trial-and-error method of examining all alloy compositions because there are so many potential HEAs, each with a different phase and set of attributes. It becomes necessary to determine the optimum combinations of components that influence phase development in order to efficiently select HEAs with desirable features. As a result, precise phase prediction becomes crucial for comprehending the characteristics and behavior of HEAs. In previous studies, bagging algorithms were commonly used to predict the phases and crystal structure of HEAs. However, the prediction accuracy achieved in those studies was found to be comparatively lower than what we have accomplished in our research.

To enhance the predictive performance and accuracy, we took a different approach and utilized five boosting algorithms such as gradient boosting, AdaBoost, XGBoost, LightGBM, and CatBoost. Boosting algorithms are known for their sequential and adaptive learning processes, which enable them to progressively improve the model's predictions. As a result of employing these boosting algorithms, a substantial increase in prediction accuracy is observed, surpassing the outcomes obtained in previous studies that relied on bagging techniques.

The adoption of these advanced boosting algorithms has proven to be a significant step forward in accurately predicting the phases and crystal structure of HEAs as well as reducing training-testing time to perform the algorithm. Our findings demonstrate the superiority of boosting over bagging when it comes to achieving higher prediction accuracy, showcasing the potential of these algorithms in the domain of material science and alloy design. In this research study, we conduct a comprehensive investigation into the computational efficiency of popular boosting algorithms for ML tasks. Specifically, we explore the training and testing times associated with these algorithms to assess their practical feasibility for real-world applications. Our research aims to identify the most time-effective method that strikes a balance between accuracy and computational speed. Table 6 presents the training and testing times for various boosting algorithms, revealing a notable advantage in computational efficiency, particularly with XGBoost. The results demonstrate that XGBoost significantly outperforms other methods, making it highly time-effective for model calculations in our research. However, the principal aim of our study is to develop and sort out the best effective ML framework for the novel design of HEAs.

3.1 Prediction of phases:

A comprehensive dataset consisting of 1345 different HEAs with varying compositions was gathered for phase prediction such as SS, IM, SS+IM, and AM. Out of the total dataset, 705 samples were selected to predict the crystal structure, utilizing four essential thermodynamic and configurational parameters. To provide a clear visualization of the phase distribution**,** a histogram was generated, depicting the total number of occurrences for each phase in Fig. 7.a. To ensure a proper evaluation of the models, the entire dataset was split into training and testing subsets, maintaining an 80:20 ratios as shown in Fig. 7.b. Results of the different ML algorithms used for phase prediction were recorded in a table, showcasing their respective accuracies as shown in Table 4.

These findings suggest that our approach with the selected ML algorithms has yielded promising results in phase prediction for HEAs, outperforming some of the earlier studies [11-13,30]. The utilization of the specified thermodynamic and configurational parameters, along with the proper dataset splitting, has contributed to the success and reliability of our models. In our study, XGBoost shows the highest performance accuracy of 94.05% for phase prediction. LightGBM and CatBoost also show decent accuracy for the prediction of phases which is above 90%. The XGBoost shows the best results when performing training, XGBoost effectively minimizes the loss function using a gradient-based optimization approach. As we have used a large dataset, XGBoost helps in giving minority classes greater weights, enhancing the model's capacity to detect uncommon occurrences. In real-world situations, imbalanced datasets are widespread. XGBoost offers tools for handling them. In Table 7, the comparison study of other algorithms for phase prediction is shown.

3.2 Confusion matrix of XGBoost classifier for prediction of phases:

In context of our study, it is a problem of multi-class labels. The heatmap function can be used to visualize the confusion matrix, as shown in Fig. 8. Here all the diagonal elements show both the true or actual values are correctly classified with the predicted values. From the figure it can be shown that 41 AM, 50 IM, 107 SS, and 55 SS+IM (Total 253) are correctly classified among a total of 269 HEAs. 8 SS phases were wrongly classified as SS+IM, 2 IM phases were wrongly predicted as SS, 3 IM were wrongly predicted as SS+IM, 1 SS+IM phase was wrongly classified

as IM phase and another SS+IM was wrongly predicted only as SS. This classification technique leads to an accuracy of (253/269) ×100 = 94.05%

3.3 Prediction of crystal structure:

A comprehensive dataset comprising 705 different HEAs with diverse compositions was meticulously collected to facilitate the prediction of crystal structures such as FCC, BCC, FCC+BCC, and multiphase. To present a clear visual representation of crystal structure distribution, a histogram was generated as shown in Fig. 9.a, offering valuable insights into the occurrence frequency of each phase. To ensure a rigorous evaluation of the models, the entire dataset was methodically divided into training and testing subsets, maintaining a precise 80:20 ratio, as illustrated in Fig. 9.b. The outcomes of the ML algorithms utilized for crystal structure prediction were meticulously documented in a tabular format shown in Table 5, showcasing their respective accuracies. These compelling findings suggest that our approach, employing the selected ML algorithms, has yielded highly promising results in accurately determining crystal structures for HEAs, surpassing the performance of some earlier studies [15,17,30]. A comparison study of different algorithms for crystal structures prediction is shown in Table 8. The successful integration of specific thermodynamic and configurational parameters, coupled with the meticulous dataset splitting, has significantly contributed to the robustness and reliability of our models. Notably, LightGBM emerged as the top-performing algorithm, attaining an impressive accuracy of 90.07% for crystal structure prediction.

3.4 Confusion matrix of LightGBM classifier for prediction of crystal structures:

For determining the accuracy of crystal structure prediction, a confusion matrix is employed here. Each element along the diagonal represents the number of instances correctly classified, where the predicted values align with the true or actual values**.** Fig. 10 shows a heatmap representation of the confusion matrix pertaining to the LightGBM classifier's predictions for the crystal structure of HEAs. In this case, the confusion matrix shows that out of the total 141 HEAs, 47 BCC, 20 FCC, 10 FCC+BCC, and 50 multiphases were correctly classified, summing up to a total of 127 accurately predicted HEAs. Specifically, 3 FCC structures were misclassified as FCC+BCC, 7 BCC phases were improperly classified as multiphase, 2multiphases were inaccurately categorized

as BCC, and 1multiphase phase was falsely projected as FCC+BCC. Despite these errors in classification, the method's overall accuracy was (127/141) × 100=90.07%.

3.5 Selection of features importance using XGBoost classifier:

The calculation of scores for each input feature in a particular model is a component of feature significance techniques. These ratings show the relative "importance" of each feature in affecting the predictions made by the model. The model's capacity to predict the target variable is thought to be more significantly impacted by a feature with a higher score. Here, the feature importance diagram is shown in Fig. 11 using the XGBoost classifier which shows that $\Delta\chi$ plays the most important role in predicting the phase as well as crystal structures of HEAs. In other words, by calculating the feature importance it is found that $\Delta\chi$ is the most important feature of our model whereas mixing enthalpy (ΔH_{mix}) is the least important feature of our model. The results of our study indicate a clear hierarchy in the accuracy of the model for phase selection, with $\Delta\chi$, δ, ΔS_{mix}, VEC, and ΔH_{mix} following a decreasing order of importance. Among these parameters, $\Delta\chi$, δ, and ΔS_{mix} stands out as the most influential factors in determining phase selection in HEAs design. This suggests that considering these three features are crucial for achieving accurate predictions. However, it is worth noting that there is some inconsistency in previous studies regarding the most critical parameter for controlling the model's accuracy. Some studies have highlighted VEC as the primary driver [13], while others have emphasized δ [11].

3.6 ROC curve for classification:

Here, we are dealing with a multiclass problem where we can see that the ROC curve for class AM is constructed by considering the classification of instances belonging to class AM against the combination of classes not belonging to class AM and the same for other classes. As a part of analysis, we have illustrated the ROC curve for the prediction of phases as shown in Fig. 12.a. The ROC curve is drawn using the XGBoost classifier for the prediction of phases and the value of the AUC of ROC curve is 1 for AM class, 0.98 for the other three classes such as IM, SS, and SS+IM. The AUC value 1 indicates that the classifier accurately classifies the AM phases from other phases. Also, for other classes, the value is very high which is 0.98 which indicates a high accuracy in classification of phases.

On the other hand, the LightGBM classifier is used for drawing the ROC for predicting the crystal structure which is shown in Fig. 12.b. We can see that the AUC value is highest for BCC and mixed FCC+BCC which is 0.99, 0.98 for FCC, and 0.97 for multiphase. These values show that the crystal structures are calefied with high AUC values. In this case, we obtained an AUC value close to 1, which signifies that the classifier's ability to distinguish between different classes is very close to the optimal level, making it an excellent performer in the classification task.

3.7 Role of feature parameters in the prediction of phases:

To get useful and accurate results, it's important to choose alloy features effectively. These qualities serve as a representation of the alloy's or the system's basic properties. The method of distinct phases in the alloy is greatly influenced by a number of thermodynamic, configurational, and electronic characteristics, including $\Delta\chi$, ΔS_{mix}, ΔH_{mix} and VEC. Empirical guidelines have been produced to direct the formation of SS, with conditions like $\Omega \geq 1.1$ and $\delta \leq 6.6\%$. Despite of these guidelines, it is still difficult to distinguish between phases accurately, especially when they are mixed [77]. Each parameter and the output have been sought to be related by researchers and ML plays a vital role in correlating the feature parameters. Fig. 13. (a, b, c, d) demonstrates the influence of the four thermodynamic and configurational parameters on ΔH_{mix} for phase stability of HEAs. These figures specifically aim to uncover the underlying rules that govern the formation of three key phases: AM, SS, IM, and SS+IM. From the figure it is clear that SS phases form when VEC is between 4 to 11, $\Delta\chi$ is in the range of 0 to 26, ΔS_{mix} ranges from 9 to 16 and ΔH_{mix} is between -1 to 27. On the other hand, the AM phase forms when VEC is slightly positive ($8 > VEC > 3$) and, $\Delta\chi$ is between 0 to 27, ΔS_{mix} ranges from 5 to 14 and ΔH_{mix} is between 3 to 44 which is very long range. Here we can see that the Intermetallic phase forms when VEC varies in a lower range ($0 < VEC < 9$) and $\Delta\chi$ ranges from 0 to 32, ΔS_{mix} lies between 1 to 16, and ΔH_{mix} lies between 0 to 35. The mixture of SS and IM phases is also inflicted by the thermodynamic and configurational parameters. This phase forms when $4 < VEC < 10$, $0 < \Delta\chi < 25$, $9 < \Delta S_{mix} < 16$, $0 < \Delta H_{mix} < 25$.

3.8 Role of feature parameters in the prediction of crystal structures:

A methodical approach was used to effectively discover the effects of factors on the crystal structure formation of the solid solution phase (BCC, FCC, FCC+BCC, and multiphase). Each

time, only one of the five parameters was changed, leaving the other four unchanged. Using this technique, it was possible to examine each parameter's contribution to the crystal structure of the solid solution phase in more detail. From the Fig. 14. (a, b, c, d) it can be shown that BCC structure forms when VEC varies from 4 to 9 and $\Delta\chi$ is slightly negative i.e., $-0.1 < \Delta\chi < 0.25$ and, ΔS_{mix}ranges from $9 < \Delta S_{mix} < 14$ whereas, ΔH_{mix} is in between 0 to 17. On the other hand, FCC structure forms when VEC is between 7 to 10, $\Delta\chi$ is between 0 to 0.25 which is slightly positive, ΔS_{mix} varies from 9 to 15 and ΔH_{mix} ranges from 0 to 10. We have also shown that mixed FCC+BCC forms when VEC varies relatively in the short range i.e., 6.5 to 9 $\Delta\chi$ varies in the very short range i.e., 0 to 0.1. ΔS_{mix} also varies in a very short range. $11 < \Delta S_{mix} < 13.5$ whereas ΔH_{mix} varies in a large range as compared to others ($0 < \Delta S_{mix} < 17$). For multiphase, VEC varies from 4 to 10, $\Delta\chi$ varies from 0 to 0.25 which is a very short range, ΔS_{mix} varies comparatively in a large range i.e., 9 to 16 whereas, ΔH_{mix} varies from 0 to 25 which is a very long range. The mixing entropy serves as an indicator of the system's complexity, where higher values suggest a greater difficulty in establishing an ordered structure [78]. From this perspective, a high mixing entropy promotes the formation of random SS or partially ordered SS phases. However, it should be noted that merely meeting the criteria of a high mixing entropy is insufficient to create SS phases in HEAs [39]**.** On the other hand, in order to promote the formation of SS phases, the formation of an AM phase must be suppressed. This is where additional requirements, such as δ and ΔH_{mix}, come into play. In essence, the interplay of these parameters governs the complexity and organization of the system, impacting the formation of various phases and crystal structures. While a high mixing entropy encourages disorder structure, other factors like atomic size differences and mixing enthalpy play crucial roles in steering the system towards forming SS phases instead of AM ones. The difference in atomic sizes creates a strain on the atoms, leading to localized elastic deformation. Additionally, the significance of mixing enthalpy is associated with the formation of clusters. A lower mixing enthalpy facilitates the creation of chemically ordered clusters, which in turn hinders the formation of solid solutions. This suggests that the preference for certain structures is influenced by the energy associated with mixing, impacting the likelihood of forming ordered arrangements or disordered solid solutions. From our study, it is revealed that electronegativity plays a different role in the formation of crystal structure. It is observed that BCC forms when $\Delta\chi$ varies in a large range ($-0.1 < \Delta\chi < 0.5$) as compared to when FCC is formed ($0 < \Delta\chi < 0.25$) which is almost half of VEC of BCC formation. Here,

the present study depicts the importance of $\Delta\chi$ for the determination of crystal structure which appears to be more effective and fundamental.

4 Conclusion:

When aiming to select an appropriate HEA with specific desired properties, the key lies in identifying the precise blend of elements that significantly influences phase development. As a result, accurately determining the present phase and its crystal structure are vital for monitoring alloy characteristics and behavior. Hence, accurate phase prediction stands as a pivotal element in the process of designing novel alloys. This research undertook phase prediction by leveraging a comprehensive database encompassing 1345 experimental alloy compositions, accompanied by their thermodynamic and configurational attributes, alongside the associated phases. In terms of comprehensive precision, the XGBoost and LightGBM classifiers exhibited superior performance compared to the other utilized boosting algorithms when evaluated using the top four identified predictive features. In the conducted research, the XGBoost algorithm demonstrated a notable accuracy of 94.05% in predicting phases, while the LightGBM algorithm exhibited a commendable accuracy of 90.07% in classifying crystal structures. This comparative analysis highlights that the multiclass performance approach introduced in this study attains elevated levels of accuracy in contrast to previous investigations within the same domain. In essence, we have successfully predicted phases and their crystal structures present in HEAs based on their compositions. In contrast to conventional ML techniques, we omitted the complex task of feature computation and selection using the Pearson correlation coefficient. The investigation presents an organized boosting ML framework aimed at resolving the multiclass phase classification issue, even in the presence of numerous diverse observations and input parameters that exhibit heterogeneity. In conclusion, this study is anticipated to offer valuable insights for the formulation and prediction of phases in novel HEAs through the utilization of ML techniques. In this work, we harnessed the power of boosting algorithms to effectively minimize both time and computational expenses, a novel approach that had not been previously explored.

Credit authorship contribution statement

Debsundar Dey: Investigation, Software, Writing – original draft, Validation. **Suchandan Das:** Investigation, Software, Resources, Validation. **Anik Pal:** Writing – review and editing, Resources, Validation. **Santanu Dey:** Resources, Validation. **Chandan Kumar Raul:** Conceptualization, Resources, Methodology, Visualization, Writing- Original draft, Supervision, Validation. **Arghya Chatterjee:** Supervision, Conceptualization, Methodology, Visualization, Validation.

Declaration of competing interest

The authors declare that they have no competing financial interests.

Acknowledgments

DD acknowledges the Indian Institute of Science, Bengaluru, India for financial support. SD acknowledges NIT Silchar for Institute Fellowship. CKR and AC acknowledge NIT Durgapur for Research Facilities.

Availability of data

Data will be made available on reasonable request.

References:

1. Lu, Z.P., Wang, H., Chen, M.W., Baker, I., Yeh, J.W., Liu, C.T. and Nieh, T.G., 2015. An assessment on the future development of high-entropy alloys: Summary from a recent workshop. *Intermetallics*, *66*, pp.67-76.

2. Ye, Y.F., Wang, Q., Lu, J., Liu, C.T. and Yang, Y., 2016. High-entropy alloy: challenges and prospects. *Materials Today*, *19*(6), pp.349-362.

3. Zhang, Y., Lu, Z.P., Ma, S.G., Liaw, P.K., Tang, Z., Cheng, Y.Q. and Gao, M.C., 2014. Guidelines in predicting phase formation of high-entropy alloys. *Mrs Communications*, *4*(2), pp.57-62.

4. Toda-Caraballo, I. and Rivera-Díaz-del-Castillo, P.E., 2015. Modelling solid solution hardening in high entropy alloys. Acta Materialia, 85, pp.14-23.

5. King, D.J.M., Middleburgh, S.C., McGregor, A.G. and Cortie, M.B., 2016. Predicting the formation and stability of single phase high-entropy alloys. *Acta Materialia*, *104*, pp.172-179.

6. Sheng, G.U.O. and Liu, C.T., 2011. Phase stability in high entropy alloys: Formation of solid-solution phase or amorphous phase. *Progress in Natural Science: Materials International*, *21*(6), pp.433-446.

7. Chattopadhyay, C., Prasad, A. and Murty, B.S., 2018. Phase prediction in high entropy alloys–A kinetic approach. *Acta Materialia*, *153*, pp.214-225.

8. ÖZKAN, D. and KARAOĞLANLI, C., 2021. High Entropy Alloys: production, properites and utilization areas. *El-Cezeri*, *8*(1), pp.164-181.

9. Agarwal, A. and Prasada Rao, A.K., 2019. Artificial intelligence predicts body-centered-cubic and face-centered-cubic phases in high-entropy alloys. *Jom*, *71*(10), pp.3424-3432.

10. Gao, M.C., Yeh, J.W., Liaw, P.K. and Zhang, Y. eds., 2016. High-entropy alloys: fundamentals and applications. Springer.

11. Huang, W., Martin, P. and Zhuang, H.L., 2019. Machine-learning phase prediction of high-entropy alloys. *Acta Materialia*, *169*, pp.225-236.

12. Risal, S., Zhu, W., Guillen, P. and Sun, L., 2021. Improving phase prediction accuracy for high entropy alloys with machine learning. *Computational Materials Science*, *192*, p.110389.

13. Islam, N., Huang, W. and Zhuang, H.L., 2018. Machine learning for phase selection in multi-principal element alloys. *Computational Materials Science*, *150*, pp.230-235.

14. Miracle, D.B. and Senkov, O.N., 2017. A critical review of high entropy alloys and related concepts. *Acta Materialia*, *122*, pp.448-511.

15. Zhang, Y., Wen, C., Wang, C., Antonov, S., Xue, D., Bai, Y. and Su, Y., 2020. Phase prediction in high entropy alloys with a rational selection of materials descriptors and machine learning models. *Acta Materialia*, *185*, pp.528-539.

16. William F.. Smith and Hashemi, J., 2006. Foundations of materials science and engineering. Mcgraw-Hill Publishing.

17. Machaka, R., 2021. Machine learning-based prediction of phases in high-entropy alloys. Computational Materials Science, 188, p.110244.

18. Troparevsky, M.C., Morris, J.R., Kent, P.R., Lupini, A.R. and Stocks, G.M., 2015. Criteria for predicting the formation of single-phase high-entropy alloys. *Physical Review X*, *5*(1), p.011041.

19. Abu-Odeh, A., Galvan, E., Kirk, T., Mao, H., Chen, Q., Mason, P., Malak, R. and Arróyave, R., 2018. Efficient exploration of the high entropy alloy composition-phase space. *Acta Materialia*, *152*, pp.41-57.

20. Girzhon, V.V., Yemelianchenko, V.V., Smolyakov, O.V. and Razzokov, A.S., 2022. Analysis of structure formation processes features in high-entropy alloys of Al-Co-Cr-Fe-Ni system during laser alloying. *Results in Materials*, *15*, p.100311.

21. Abdelghany, A.W., Jaskari, M., Hamada, A.S., Järvenpää, A., El-Hofy, H.A., Chiba, A. and Gepreel, M.A.H., 2022. Hot deformation behavior and constitutive modeling of a cost-effective Al8Cr12Mn25Ni20Fe35 high-entropy alloy. *Journal of Alloys and Compounds*, *928*, p.167028.

22. Sanchez, J.M., Vicario, I., Albizuri, J., Guraya, T. and Garcia, J.C., 2019. Phase prediction, microstructure and high hardness of novel light-weight high entropy alloys. *Journal of Materials Research and Technology*, *8*(1), pp.795-803.

23. Tian, F., Delczeg, L., Chen, N., Varga, L.K., Shen, J. and Vitos, L., 2013. Structural stability of NiCoFeCrAl x high-entropy alloy from ab initio theory. *Physical Review B*, *88*(8), p.085128.

24. Li, Y. and Guo, W., 2019. Machine-learning model for predicting phase formations of high-entropy alloys. *Physical Review Materials*, *3*(9), p.095005.

25. Gao, M.C., Zhang, C., Gao, P., Zhang, F., Ouyang, L.Z., Widom, M. and Hawk, J.A., 2017. Thermodynamics of concentrated solid solution alloys. *Current Opinion in Solid State and Materials Science*, *21*(5), pp.238-251.

26. Jiang, C. and Uberuaga, B.P., 2016. Efficient ab initio modeling of random multicomponent alloys. *Physical review letters*, *116*(10), p.105501.

27. Choudhury, A., 2021. The role of machine learning algorithms in materials science: A state of art review on industry 4.0. *Archives of Computational Methods in Engineering*, *28*(5), pp.3361-3381.

28. Kaufmann, K. and Vecchio, K.S., 2020. Searching for high entropy alloys: A machine learning approach. *Acta Materialia*, *198*, pp.178-222.

29. Hou, S., Li, Y., Bai, M., Sun, M., Liu, W., Wang, C., Tetik, H. and Lin, D., 2022. Phase prediction of high-entropy alloys by integrating criterion and machine learning recommendation method. *Materials*, *15*(9), p.3321.c

30. Mandal, P., Choudhury, A., Mallick, A.B. and Ghosh, M., 2023. Phase prediction in high entropy alloys by various machine learning modules using thermodynamic and configurational parameters. *Metals and Materials International*, *29*(1), pp.38-52.

31. Qi, J., Cheung, A.M. and Poon, S.J., 2020. Navigating the Complex Compositional Landscape of High-Entropy Alloys. *arXiv preprint arXiv:2011.14403*.

32. Chanda, B., Jana, P.P. and Das, J., 2021. A tool to predict the evolution of phase and Young's modulus in high entropy alloys using artificial neural network. *Computational Materials Science*, *197*, p.110619.

33. Xiong, J., Shi, S.Q. and Zhang, T.Y., 2021. Machine learning of phases and mechanical properties in complex concentrated alloys. *Journal of Materials Science & Technology*, *87*, pp.133-142.

34. Poletti, M.G. and Battezzati, L.J.A.M., 2014. Electronic and thermodynamic criteria for the occurrence of high entropy alloys in metallic systems. *Acta materialia*, *75*, pp.297-306.

35. Yang, X. and Zhang, Y., 2012. Prediction of high-entropy stabilized solid-solution in multi-component alloys. *Materials Chemistry and Physics*, *132*(2-3), pp.233-238.

36. Takeuchi, A. and Inoue, A., 2005. Classification of bulk metallic glasses by atomic size difference, heat of mixing and period of constituent elements and its application to characterization of the main alloying element. *Materials transactions*, *46*(12), pp.2817-2829.

37. Ye, Y.F., Wang, Q., Lu, J., Liu, C.T. and Yang, Y., 2016. High-entropy alloy: challenges and prospects. *Materials Today*, *19*(6), pp.349-362.

38. Singh, S., Katiyar, N.K., Goel, S. and Joshi, S.N., 2023. Phase prediction and experimental realisation of a new high entropy alloy using machine learning. Scientific Reports, 13(1), p.4811.

39. Sheng, G.U.O. and Liu, C.T., 2011. Phase stability in high entropy alloys: Formation of solid-solution phase or amorphous phase. *Progress in Natural Science: Materials International*, *21*(6), pp.433-446.

40. Juan, Y.F., Li, J., Jiang, Y.Q., Jia, W.L. and Lu, Z.J., 2019. Modified criterions for phase prediction in the multi-component laser-clad coatings and investigations into microstructural evolution/wear resistance of FeCrCoNiAlMox laser-clad coatings. *Applied Surface Science*, *465*, pp.700-714.

41. Chawla, N.V., Bowyer, K.W., Hall, L.O. and Kegelmeyer, W.P., 2002. SMOTE: synthetic minority over-sampling technique. *Journal of artificial intelligence research*, *16*, pp.321-357.

42. Blagus, R. and Lusa, L., 2013. SMOTE for high-dimensional class-imbalanced data. BMC bioinformatics, 14, pp.1-16.

43.Mukherjee, M. and Khushi, M., 2021. SMOTE-ENC: A novel SMOTE-based method to generate synthetic data for nominal and continuous features. Applied System Innovation, 4(1), p.18.

44. Blagus, R. and Lusa, L., 2013. SMOTE for high-dimensional class-imbalanced data. *BMC bioinformatics*, *14*, pp.1-16.

45. Guo, Q., Xu, X., Pei, X., Duan, Z., Liaw, P.K., Hou, H. and Zhao, Y., 2022. Predict the phase formation of high-entropy alloys by compositions. *Journal of Materials Research and Technology*.

46. Cohen, I., Huang, Y., Chen, J. and Benesty, J., 2009. *Noise reduction in speech processing* (pp. 1-4). Springer Berlin Heidelberg.

47. Mueller, T., Kusne, A.G. and Ramprasad, R., 2016. Machine learning in materials science: Recent progress and emerging applications. *Reviews in computational chemistry*, *29*, pp.186-273.

48. Moosavi, S.M., Jablonka, K.M. and Smit, B., 2020. The role of machine learning in the understanding and design of materials. *Journal of the American Chemical Society*, *142*(48), pp.20273-20287.

49. Liu, W., Chen, Z. and Hu, Y., 2022. XGBoost algorithm-based prediction of safety assessment for pipelines. International Journal of Pressure Vessels and Piping, 197, p.104655.

50. Liang, W., Luo, S., Zhao, G. and Wu, H., 2020. Predicting hard rock pillar stability using GBDT, XGBoost, and LightGBM algorithms. *Mathematics*, *8*(5), p.765.

51. Li, M., Fu, X. and Li, D., 2020, March. Diabetes prediction based on XGBoost algorithm. In *IOP conference series: materials science and engineering* (Vol. 768, No. 7, p. 072093). IOP Publishing.

52. Song, K., Yan, F., Ding, T., Gao, L. and Lu, S., 2020. A steel property optimization model based on the XGBoost algorithm and improved PSO. *Computational Materials Science*, *174*, p.109472.

53. Burez, J. and Van den Poel, D., 2009. Handling class imbalance in customer churn prediction. *Expert Systems with Applications*, *36*(3), pp.4626-4636.

54. Hastie, T., Tibshirani, R., Friedman, J.H. and Friedman, J.H., 2009. *The elements of statistical learning: data mining, inference, and prediction* (Vol. 2, pp. 1-758). New York: springer.

55. Schapire, R.E., 2013. Explaining adaboost. In *Empirical Inference: Festschrift in Honor of Vladimir N. Vapnik* (pp. 37-52). Berlin, Heidelberg: Springer Berlin Heidelberg.

56. Hornyák, O. and Iantovics, L.B., 2023. AdaBoost Algorithm Could Lead to Weak Results for Data with Certain Characteristics. *Mathematics*, *11*(8), p.1801.

57. Natekin, A. and Knoll, A., 2013. Gradient boosting machines, a tutorial. *Frontiers in neurorobotics*, *7*, p.21.

58. Bentéjac, C., Csörgő, A. and Martínez-Muñoz, G., 2021. A comparative analysis of gradient boosting algorithms. *Artificial Intelligence Review*, *54*, pp.1937-1967.

59. Kuhn, M. and Johnson, K., 2013. *Applied predictive modeling* (Vol. 26, p. 13). New York: Springer.

60. Zhang, Y. and Haghani, A., 2015. A gradient boosting method to improve travel time prediction. *Transportation Research Part C: Emerging Technologies*, *58*, pp.308-324.

61. El-Behery, H., Attia, A.F., El-Fishawy, N. and Torkey, H., 2021. Efficient machine learning model for predicting drug-target interactions with case study for Covid-19. *Computational Biology and Chemistry*, *93*, p.107536.

62. Ke, G., Meng, Q., Finley, T., Wang, T., Chen, W., Ma, W., Ye, Q. and Liu, T.Y., 2017. Lightgbm: A highly efficient gradient boosting decision tree. *Advances in neural information processing systems*, *30*.

63. Namburu, A., Selvaraj, P. and Varsha, M., 2022. Product pricing solutions using hybrid machine learning algorithm. *Innovations in Systems and Software Engineering*, pp.1-12.

64. Pan, J., Ma, B., Hou, X., Li, C., Xiong, T., Gong, Y. and Song, F., 2022. The construction of transcriptional risk scores for breast cancer based on lightGBM and multiple omics data. *Mathematical Biosciences and Engineering*, *19*(12), pp.12353-12370.

65. Zhou, F., Pan, H., Gao, Z., Huang, X., Qian, G., Zhu, Y. and Xiao, F., 2021. Fire prediction based on catboost algorithm. *Mathematical Problems in Engineering*, *2021*, pp.1-9.

66. Prokhorenkova, L., Gusev, G., Vorobev, A., Dorogush, A.V. and Gulin, A., 2018. CatBoost: unbiased boosting with categorical features. *Advances in neural information processing systems*, *31*.

67. Hancock, J. and Khoshgoftaar, T.M., 2020, August. Medicare fraud detection using catboost. In *2020 IEEE 21st international conference on information reuse and integration for data science (IRI)* (pp. 97-103). IEEE.

68. Marom, N.D., Rokach, L. and Shmilovici, A., 2010, November. Using the confusion matrix for improving ensemble classifiers. In *2010 IEEE 26-th Convention of Electrical and Electronics Engineers in Israel* (pp. 000555-000559). IEEE.

69. Goutte, C. and Gaussier, E., 2005, March. A probabilistic interpretation of precision, recall and F-score, with implication for evaluation. In *European conference on information retrieval* (pp. 345-359). Berlin, Heidelberg: Springer Berlin Heidelberg.

70. Podder, P., Bharati, S., Mondal, M.R.H. and Kose, U., 2021. Application of machine learning for the diagnosis of COVID-19. In *Data science for COVID-19* (pp. 175-194). Academic Press.

71. Sokolova, M., Japkowicz, N. and Szpakowicz, S., 2006, December. Beyond accuracy, F-score and ROC: a family of discriminant measures for performance evaluation. In *Australasian joint conference on artificial intelligence* (pp. 1015-1021). Berlin, Heidelberg: Springer Berlin Heidelberg.

72. Kumar, R. and Indrayan, A., 2011. Receiver operating characteristic (ROC) curve for medical researchers. *Indian pediatrics*, *48*, pp.277-287

73. Gonçalves, L., Subtil, A., Oliveira, M.R. and de Zea Bermudez, P., 2014. ROC curve estimation: An overview. *REVSTAT-Statistical journal*, *12*(1), pp.1-20.

74. Koizumi, Y., Murata, S., Harada, N., Saito, S. and Uematsu, H., 2019, May. SNIPER: Few-shot learning for anomaly detection to minimize false-negative rate with ensured true-positive rate. In ICASSP 2019-2019 IEEE International Conference on Acoustics, Speech and Signal Processing (ICASSP) (pp. 915-919). IEEE.

75. Mishra, A., Kompella, L., Sanagavarapu, L.M. and Varam, S., 2022. Ensemble-based machine learning models for phase prediction in high entropy alloys. Computational Materials Science, 210, p.111025.

76. Zhao, D.Q., Pan, S.P., Zhang, Y., Liaw, P.K. and Qiao, J.W., 2021. Structure prediction in high-entropy alloys with machine learning. Applied Physics Letters, 118(23).

77. Zhang, L., Chen, H., Tao, X., Cai, H., Liu, J., Ouyang, Y., Peng, Q. and Du, Y., 2020. Machine learning reveals the importance of the formation enthalpy and atom-size difference in forming phases of high entropy alloys. *Materials & Design*, *193*, p.108835.

78. Greer, A.L., 1993. Confusion by design. *Nature*, *366*(6453), pp.303-304.

Table 1: Dataset of phases of HEAs.

Alloys	**VEC**	$\Delta\chi$	$\boldsymbol{\Delta H_{mix}}$	$\boldsymbol{\Delta S_{mix}}$	$\boldsymbol{\delta}$ (%)	**phase**
$CoCuFeNiSn_{0.02}$	9.4989	0.0164	5.0008	11.54	1.23	SS
$Fe_{61}B_{15}Mo7Zr_8Co7Y_2$	6.76	0.11139	-22.4832	10.3	17.141	AM
$Fe_{61}B_{15}Mo_7Zr_8Co5Y2Cr_2$	6.7	0.1124	-22.3168	10.65	17.141	AM
Al_6CuMg_4	10.16	0.07073	-0.6672	3.26	5.495	IM
$Al_{0.5}CoCrFe_2NiTi_{0.5}$	8.27833	0.06197	-5.50009	10.2	1.595	SS+IM

Table 2: Dataset of crystal structures of HEAs.

Alloys	**VEC**	$\Delta\chi$	$\boldsymbol{\Delta H_{mix}}$	$\boldsymbol{\Delta S_{mix}}$	$\boldsymbol{\delta}$ (%)	**Crystal structure**
$NiCoFeCrAl_{1.21}$	8.18648	0.05437	-4.40092	11.93	1.657	FCC
$MoNbHfZrTi_{1.5}$	4.73875	0.21458	-1.97	12	6.68	BCC
$Al_{0.5}CoCrCuFeNiTi_{1.2}$	8.7134	0.05363	1.93128	13.96	2.312	FCC+BCC+IM
$Al_{0.5}CoCrCu_{0.5}FeNiTi_{0.5}$	8.21625	0.05459	-4.20379	12.14	1.644	FCC+BCC
AlCoCrCuFeMnNi	7.71	0.07963	5.63	16.18	4.57	Multiphase

Table 3: Binary classification for accuracy estimation.

	True predicted	False predicted
False Actual	FP	FN
True Actual	TP	TN

Table 4: Representation of accuracy (%), Precision (%), Recall (%), F1-score of five different algorithms used for prediction of phases.

Classifier	**Accuracy (%)**	**Precision (%)**	**Recall (%)**	**F1 Score**
AdaBoost	78.12	77.52	79.36	0.783
XGBoost	**94.05**	**94.45**	**94.05**	**0.941**
LightGBM	92.44	93.28	91.94	0.927
CatBoost	90.12	89.69	91.46	0.904
Gradient Boosting	82.15	83.74	82.63	0.831

Table 5: Representation of accuracy (%), Precision (%), Recall (%), F1-score of five different algorithms used for prediction of crystal structures.

Classifier	**Accuracy (%)**	**Precision (%)**	**Recall (%)**	**F1 Score**
AdaBoost	67.92	68.93	67.56	0.681
XGBoost	85.45	86.12	85.86	0.859
LightGBM	**90.07**	**90.07**	**90.08**	**0.899**
CatBoost	79.60	76.95	79.98	0.783
Gradient Boosting	75.81	75.14	75.94	0.754

Table 6: It indicates the training- testing time for different classifier. From the table it is very clear that XGBoost is very time-efficient algorithm that can be used for prediction of phases and crystal structures.

Algorithm	**Training time (Sec)**	**Testing time (sec)**
XGBoost	0.92	0.98
LightGBM	1.04	1.16
AdaBoost	1.51	1.4
Gradient boosting	0.95	0.97
CatBoost	1.67	1.44

Table 7: Comparison study of different ML models for phase prediction of HEAs.

Model	**Accuracy(%)**	**Reference**
ANN	8	[11]
ANN	83	[13]
DT+SVM	93.84	[30]
RF	90.8	[75]
XGboost	**94.05**	**This study**

Table 8: Comparison study of different ML models for crystal structure prediction of HEAs.

Model	**Accuracy (%)**	**Reference**
RF	82.3	[17]
ANN	87	[76]
SVM	84.32	[30]
LightGBM	**90.07**	**This study**

Figures caption:

Figure 1: Fig. 1.a shows the unbalanced dataset of phases before applying SMOTE and Fig. 1.b shows the balanced dataset using SOMTE.

Figure 2: Fig. 2.a shows the unbalanced dataset of crystal structures before applying SMOTE and Fig. 2.b shows the balanced dataset using SOMTE.

Figure 3: Fig. 3.a indicates the heatmap of Pearson correlation coefficient matrix with original features and Fig. 3.b indicates the features after screening.

Figure 4: Fig. 4 indicates 4 × 4 scatter plot showing the correlation between various features for the phase prediction.

Figure 5: Fig. 5 indicates 4 × 4 scatter plot showing the correlation between various features for the prediction of crystal structures.

Figure 6: Fig. 6 shows the flow diagram of the different classifiers which are employed in our study to predict the phases and crystal structures of HEAs.

Figure 7: Fig. 7.a indicates the distribution of phases and Fig. 7.b indicates the training-testing distribution of the data with 80:20 ratio.

Figure 8: Fig. 8 shows the confusion matrix of XGBoost classifier algorithm for phase prediction.

Figure 9: Fig. 9.a indicates the distribution of crystal structures and Fig. 9.b indicates the training-testing distribution of the dataset with 80:20 ratio.

Figure 10: Fig. 10 shows the confusion matrix of LightGBM classifier algorithm for crystal structure prediction.

Figure 11: Fig. 11 shows the parameter importance percentage in prediction of phases.

Figure 12: Fig. 12.a shows the ROC -AUC scores for XGBoost classifier for different phase classification (AUC value is highest for AM class) and Fig. 12.b shows the ROC -AUC scores for LightGBM classifier for different crystal structure classification (AUC value is highest for both BCC and FCC+BCC).

Figure 13: Fig. 13 shows the relationship established between each input parameters to the output phases of HEAs. In Fig. 13.a shows Valence electron concentration (VEC), Fig. 13.b shows electronegativity difference ($\Delta\chi$), Fig. 13.c shows configurational entropy (ΔS_{mix}), Fig.13. d shows mixing enthalpy (ΔH_{mix}).

Figure 14: Fig. 14 shows the relationship established between each input parameters to the output crystal structures of HEAs. In Fig. 14.a shows Valence electron concentration (VEC), Fig. 14.b shows electronegativity difference ($\Delta\chi$), Fig. 14.c shows configurational entropy (ΔS_{mix}), Fig.14. d shows mixing enthalpy (ΔH_{mix}).

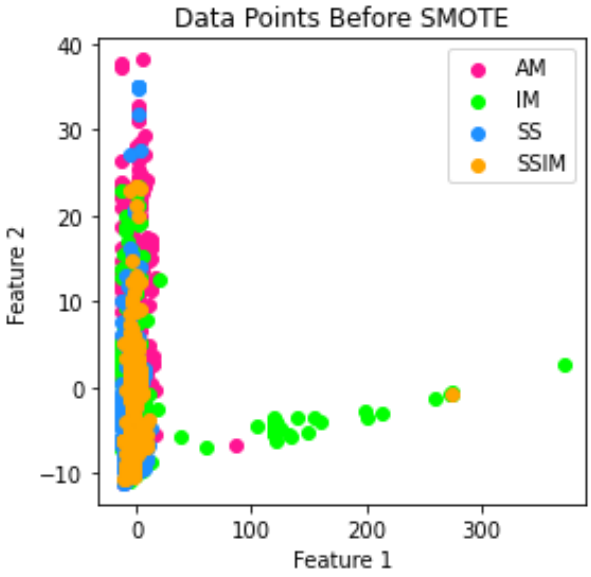

Fig. 1.a

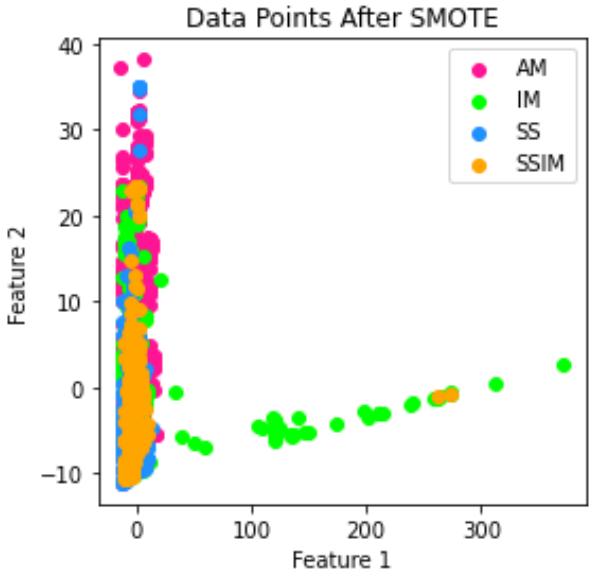

Fig. 1.b

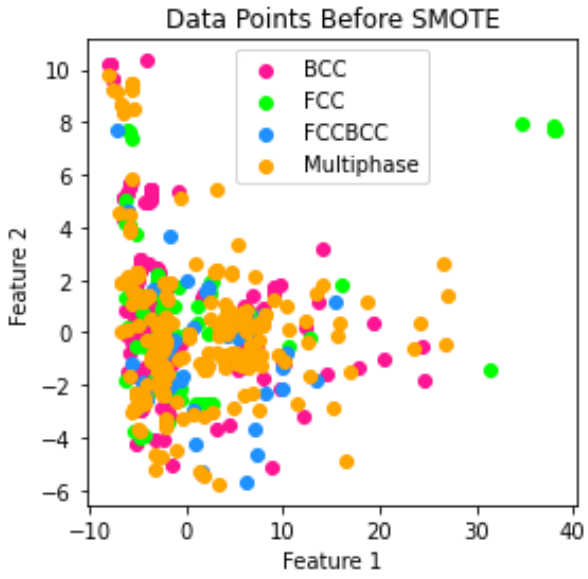

Fig. 2.a

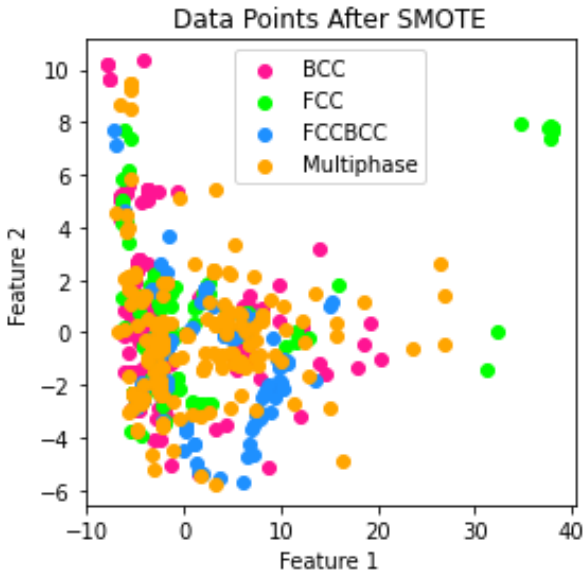

Fig. 2.b

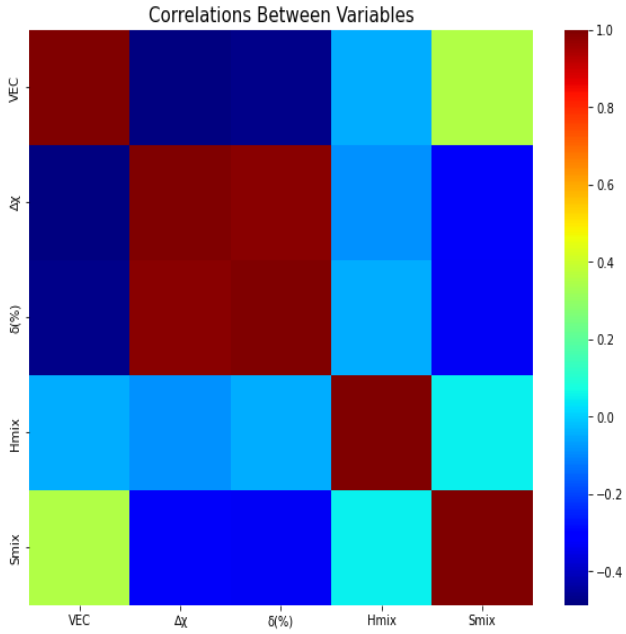

Fig. 3.a

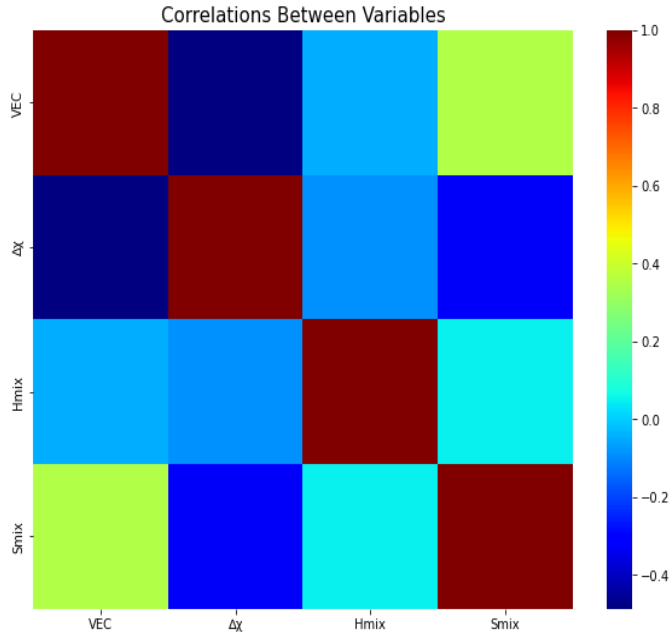

Fig. 3.b

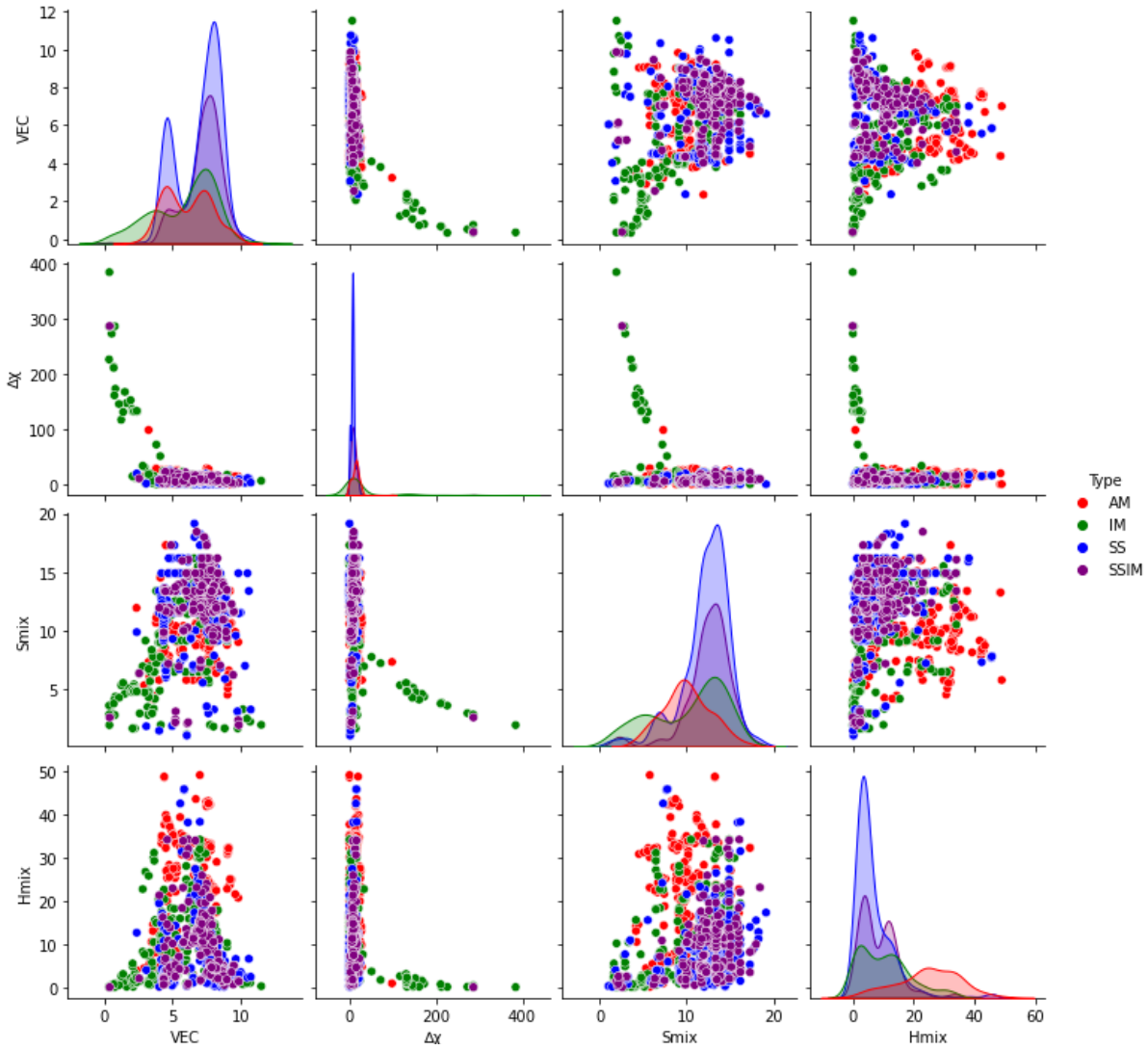

Fig. 4

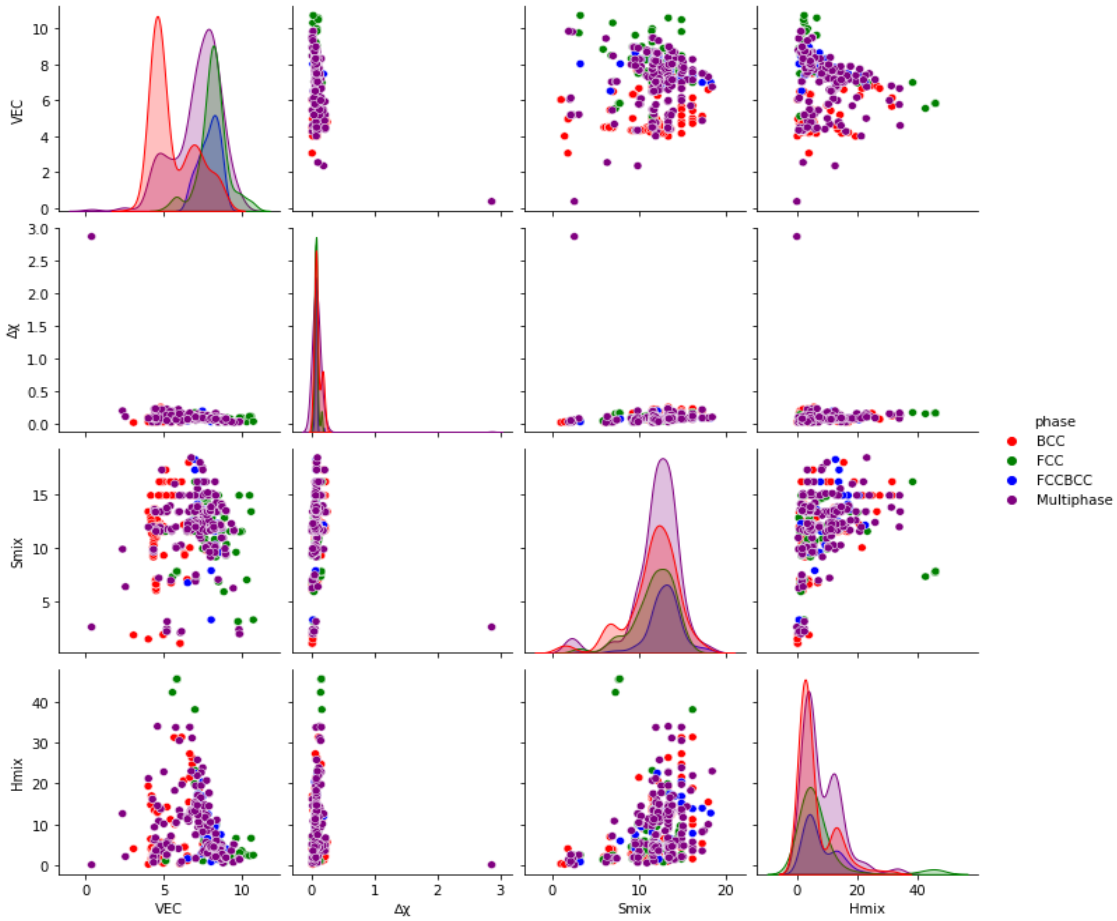
VEC
Δχ
Smix
Hmix
phase
BCC
FCC
FCCBCC
Multiphase

Fig. 5

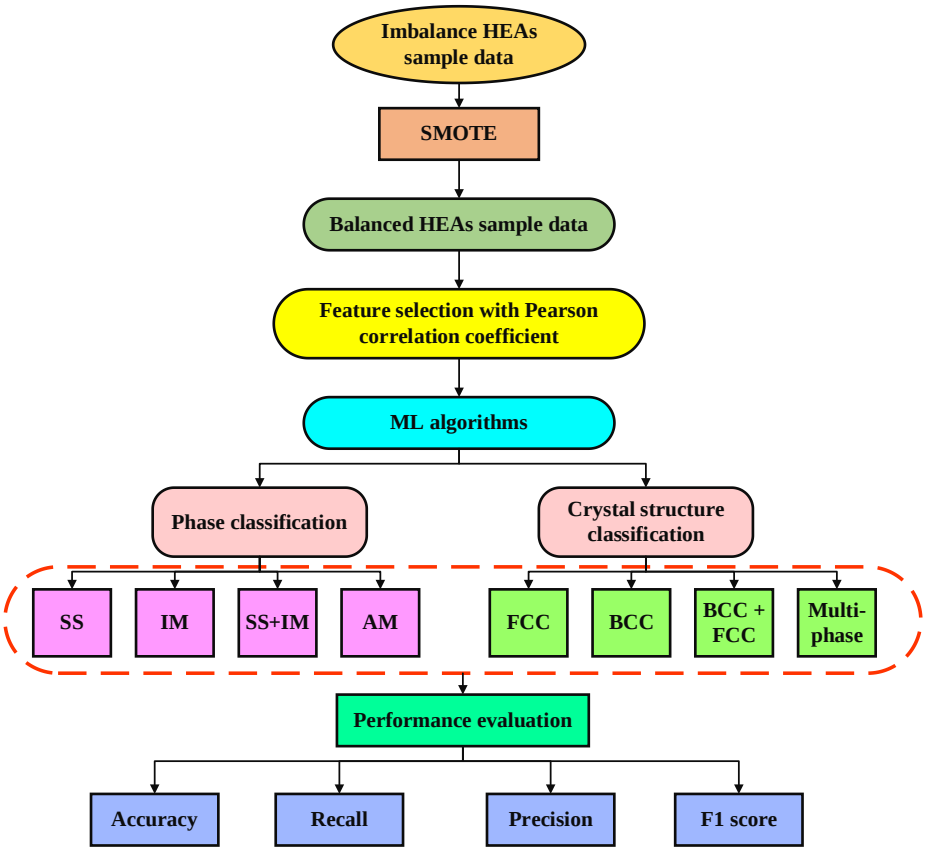
Imbalance HEAs sample data
SMOTE
Balanced HEAs sample data
Feature selection with Pearson correlation coefficient
ML algorithms
Phase classification
Crystal structure classification
SS
IM
SS+IM
AM
FCC
BCC
BCC + FCC
Multi-phase
Performance evaluation
Accuracy
Recall
Precision
F1 score

Fig. 6

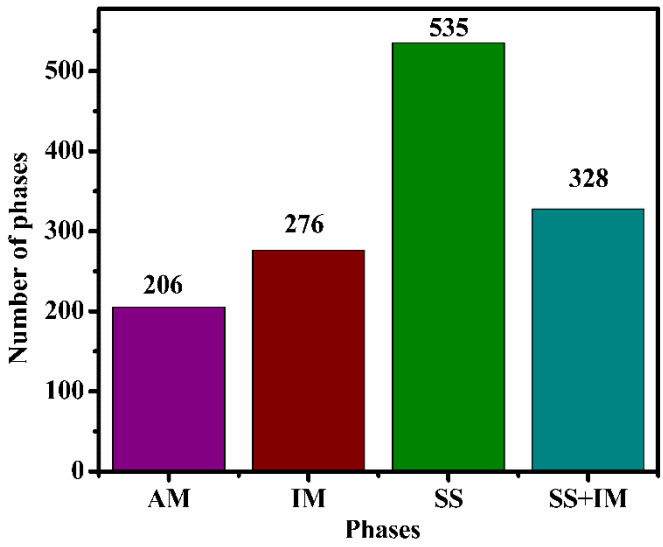

Fig. 7.a

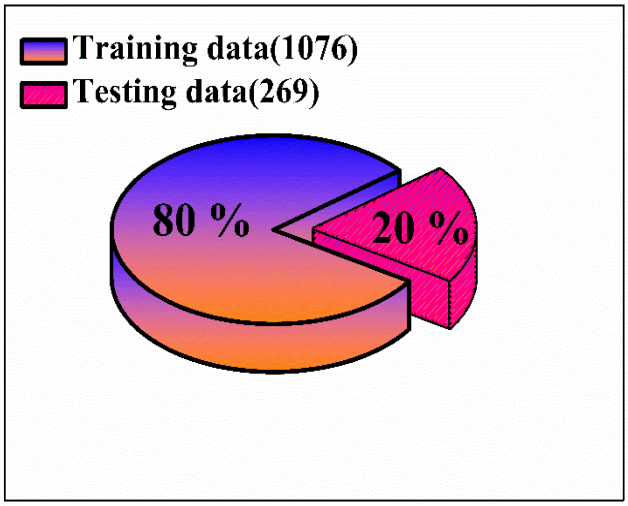

Fig. 7.b

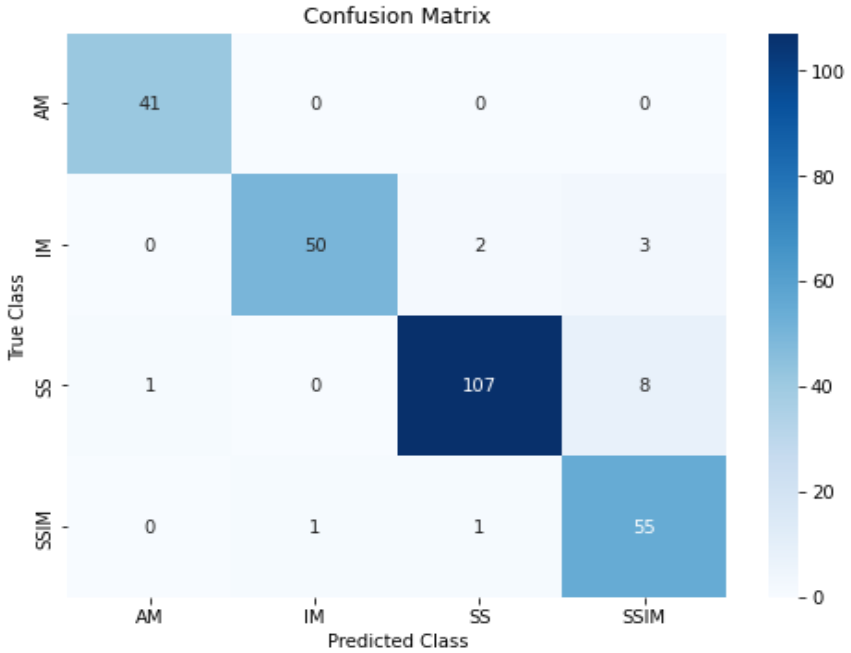

Fig. 8

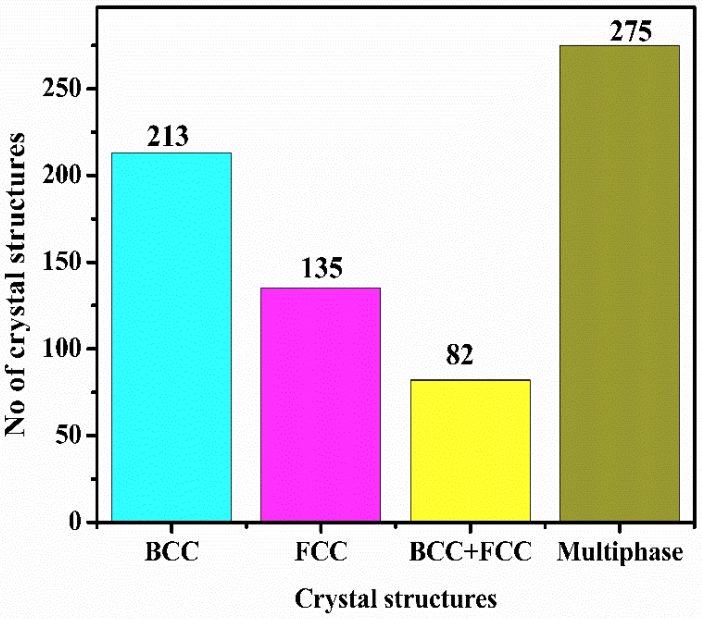

Fig. 9.a

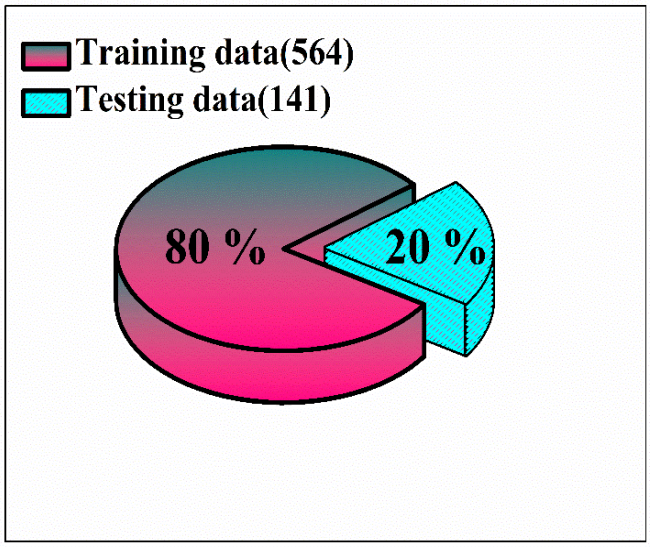

Fig. 9.b

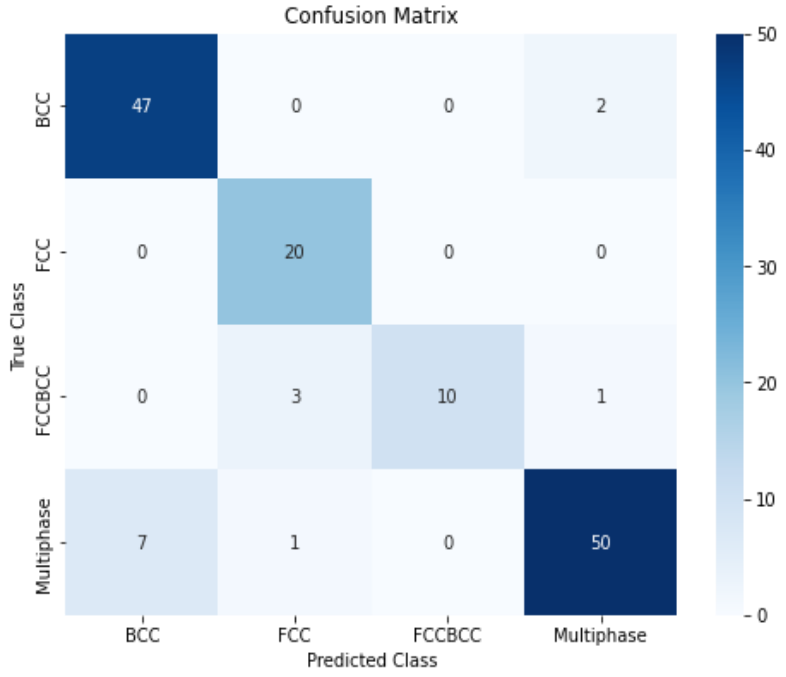

Fig. 10

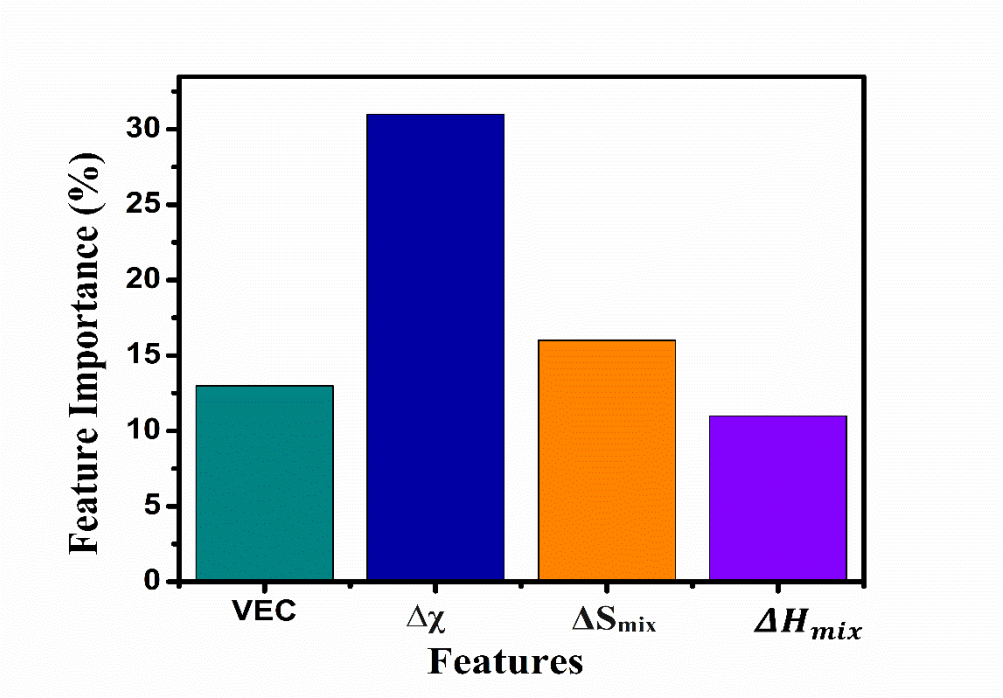

Fig. 11

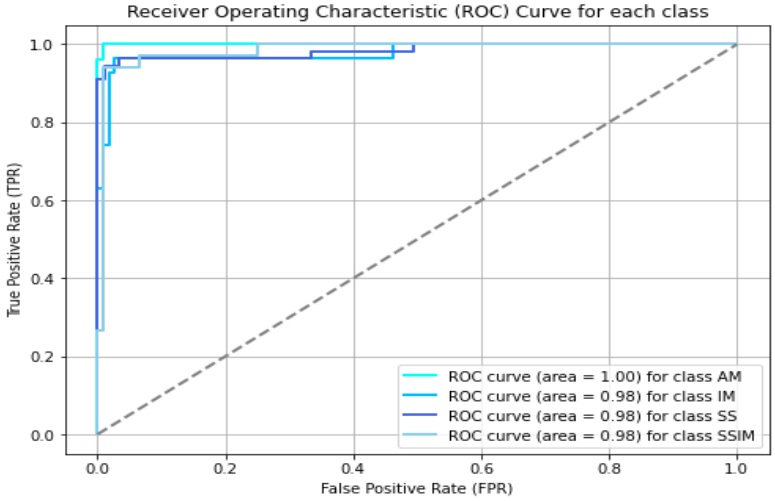

Fig. 12.a

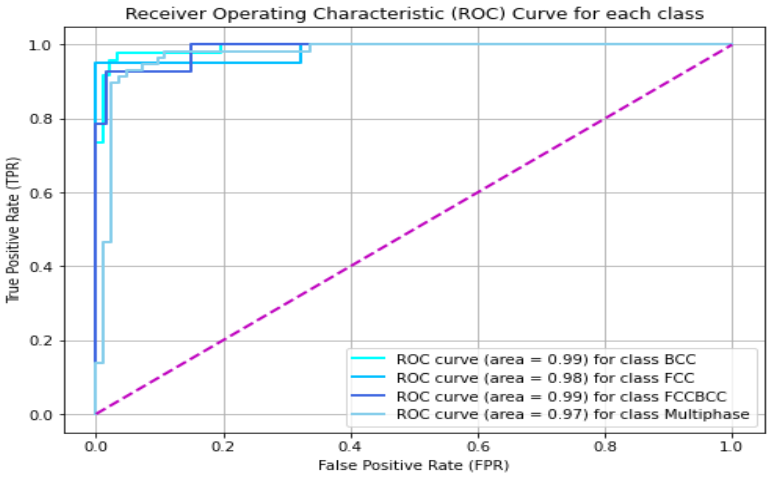

Fig. 12.b

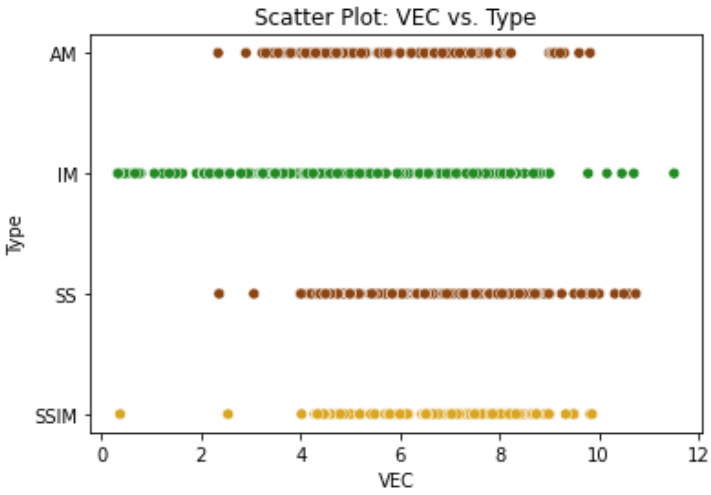

Fig. 13.a

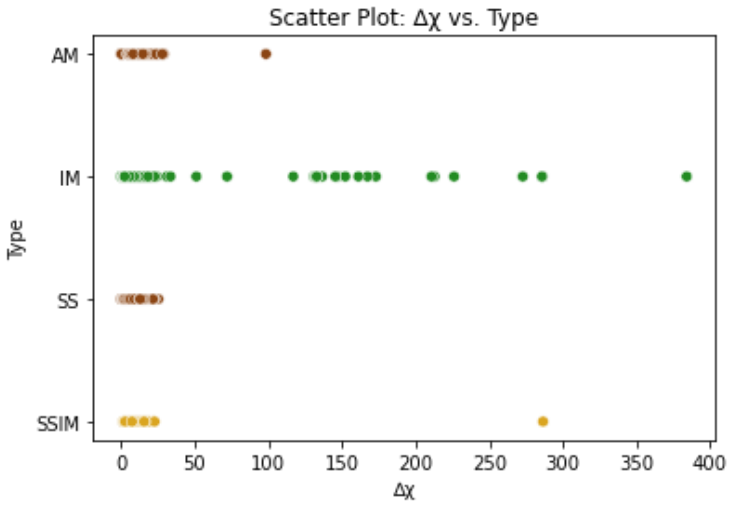

Fig. 13.b

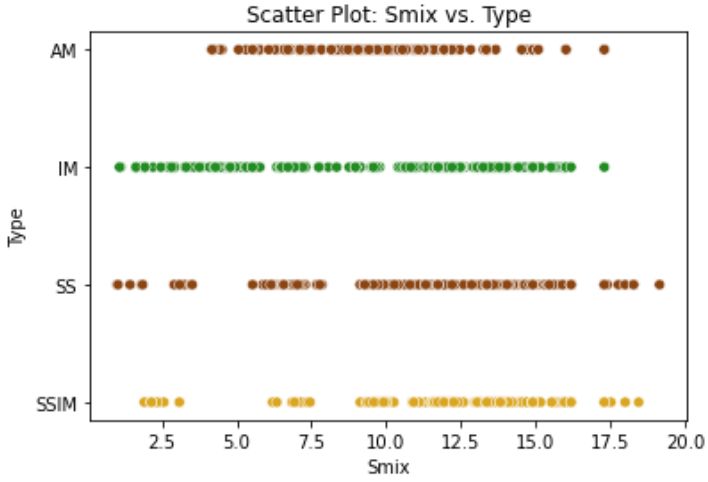

Fig. 13.c

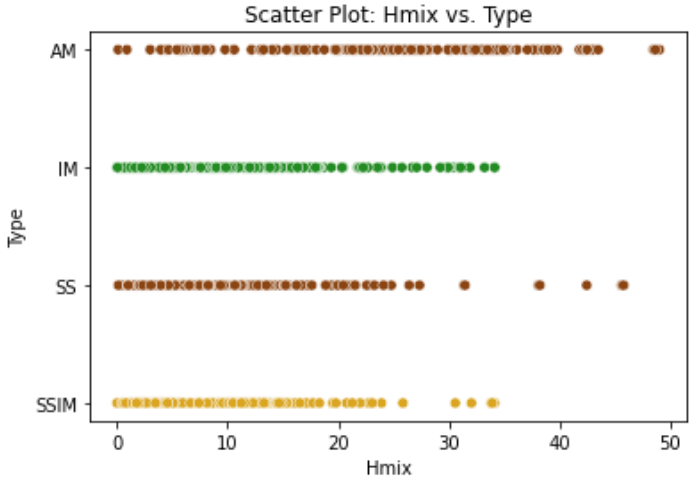

Fig. 13.d

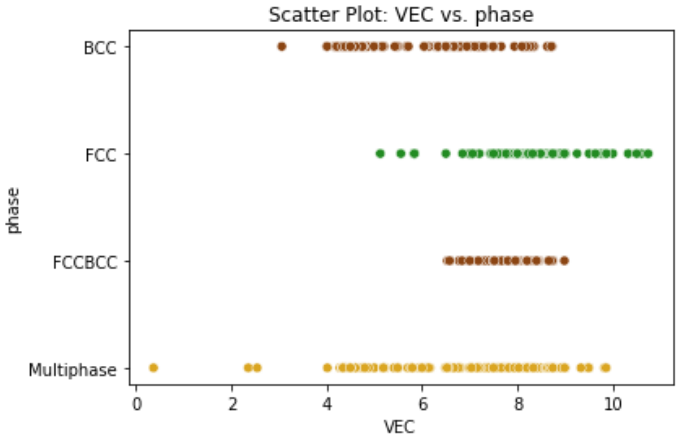

Fig. 14.a

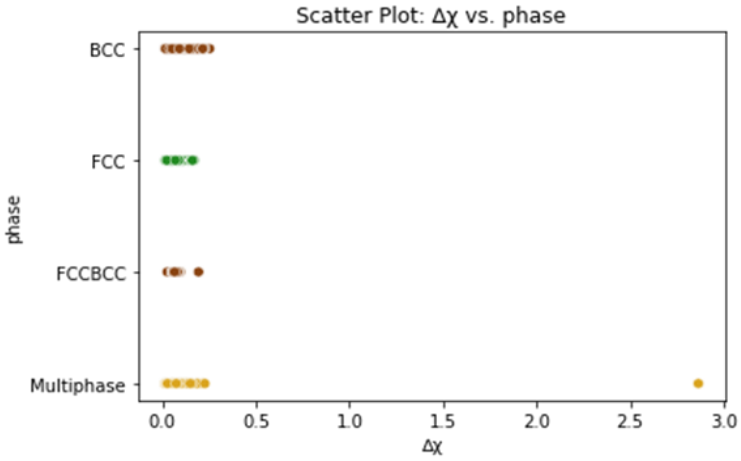

Fig. 14.b

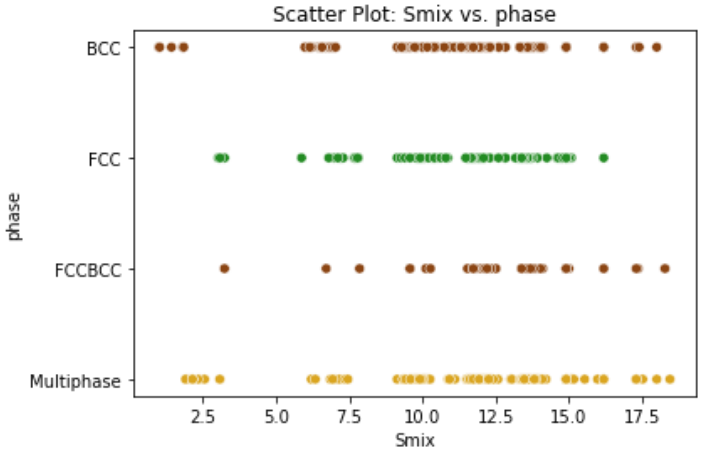

Fig. 14.c

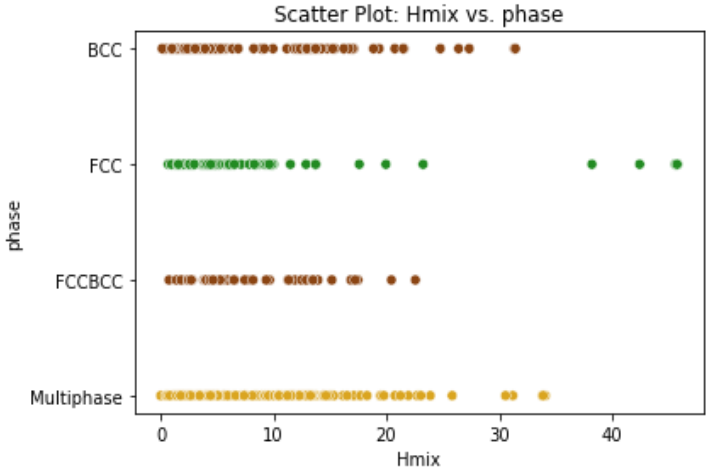

Fig. 14.d